Title
High Energy Density Lithium Metal Battery Enabled by Next Generation Solid State Electrolyte for Future Energy Storage

Author
Zhu, Dan

Publication Date
2021

Peer reviewed|Thesis/dissertation

UNIVERSITY OF CALIFORNIA

Los Angeles

High Energy Density Lithium Metal Battery Enabled by Next Generation Solid State Electrolyte for Future Energy Storage

A dissertation submitted in partial satisfaction of the

requirements for the degree Doctor of Philosophy

in Chemistry

by

Dan Zhu

2021

ABSTRACT OF THE DISSERTATION

High Energy Density Lithium Metal Battery Enabled by Next Generation Solid State Electrolyte for Future Energy Storage

by

Dan Zhu

Doctor of Philosophy in Chemistry

University of California, Los Angeles, 2021

Professor Xiangfeng Duan, Chair

Portable energy storage is of critical importance for the advance of renewable energy storage, consumer electronics, electric vehicles, and electric aviation, due to the increasingly complex and energy intensive products. Most of the mobile energy market relies on and is dominated by Li-ion battery technology, since its commercial introduction during the 1990s. However, the commercial Li-ion battery does not use lithium metal (3840 mA h g^{-1}) as anode, but instead uses graphite anode or LiC_6 (372 mA h g^{-1}) when fully charged with only ~10% capacity compared to solid lithium metal. Thus, to increase the energy density of the battery and keep up with the improvement of future electronics, incorporation of lithium metal anode will have to be realized. However, the holy grail that is lithium metal anode is plagued by numerous hindrances. The chief problem being lithium dendrite growth as the result of charge and

discharge during battery usage. The formation of lithium dendrite can result in the capacity fade of the battery due to electrode detachment, and severe safety concerns of battery short from dendrite penetrating the thin separator, and unwanted side reaction with the volatile electrolytes. These inherent problems can be addressed by incorporating solid-state electrolytes, where higher modulus can suppress the danger associated with lithium metal anode. In the first part of this thesis, we discuss the background and electrochemistry of a battery and the role of solid electrolytes compared to its liquid counterpart. In the second portion, we examine the application of nanomaterials and nanostructures in solid state electrolyte to enhance the low ionic conductivity of solid electrolyte to realize the effects of percolation pathways. In the third part, we examine the high surface area 3D network nanostructure with electronegative surface atoms that enhances ionic conductivity at the interface between the network and polymer. Lastly, we demonstrate the use of lithium trifluoromethane-bis-(sulfonyl)imide (LiTFSI) surface functionalized silica aerogel/polyethylene oxide (PEO) composite electrolyte. And its ionic conductivity (2×10^{-3} S/cm) compared to the liquid and solid counterparts. In addition, we unravel the typically neglected ionic conductivity at extremely low temperature regime.

This dissertation of Dan Zhu is approved.

Chong Liu

Alexander M. Spokoyny

Jeffrey I. Zink

Xiangfeng Duan, Committee Chair

University of California, Los Angeles

2021

Dedicated to my parents, my brother Heng,
and all my family and friends for their
unwavering support and encouragement

Dedicated to my undergraduate professors
Dr. Jess Vickery, Dr. Jason Hein, and Dr. Carrie Menke for
guiding me on the academic path

TABLE OF CONTENTS

List of Figures

Acknowledgements

I would like to use this opportunity to express my gratitude to those who have helped and supported me along my academic journey to obtain my Ph.D. First and foremost, I would like to thank my advisor, Professor Xiangfeng Duan, for his support, guidance, and mentorship during the entirety of my graduate school. When I joined the Duan lab during Summer of 2016, he provided insights, opportunities, scientific discussions into many of the projects that I participated in. As a result of his support, I went from an undergraduate student that was unsure about how to do proper research, or knowing about my future career, to an experienced independent research able to generate ideas and approaches to challenging problems, formulate my own hypothesis, proceed with the necessary experiments, and understand and interpret the results and data. I would also like to express my thanks to committee members, Professor Jeffrey I. Zink, Professor Chong Liu, and Professor Alexander Spokoyny.

During my graduate student career, there were numerous graduate students and post doctorates that contributed to my success, and I would also like to use this opportunity to express my gratitude towards. First, I would like to thank Frank Song, Daniel Baumann, Guangyan Zhong, Peiqi Wang, and Bocheng Cao for their collaborations, support, and encouragement during difficulties. Second, I would like to thank Dr. Lele Peng for his collaborations and teachings on electrolyte systems. I would like to thank Dr. Benjamin J. Papandrea, Dr. Chain Lee, and Dr. Boris Volosskiy, for teaching me the fundamentals of battery technology and electrochemistry. I would like to thank Dr. Hongtao Sun for his teaching on electrochemical impedance spectroscopy and support on research of solid-state electrolyte materials. Finally, I would like to thank all the other member of the Duan lab during my graduate career that made this achievement possible.

VITA

2012	High School Diploma Foothill High School Pleasanton, CA
2014	Transfer Student, Chemistry University of California, Merced Merced, CA
2016	Bachelor of Science, College of Chemistry University of California, Berkeley Berkeley, CA
Expected in 2021	Doctor of Philosophy in Chemistry University of California, Los Angeles Los Angeles, CA

Chapter 1. The Rise and Morph of Battery in Energy Storage Applications

1.1 Introduction, Background, and Motivation on Electrolytes for Energy Storage Applications

With the advent of mobile electronics and the continuous endeavor towards carbon neutrality, there has never been a greater need for improvements in reliable energy storage options. The modern energy storage options are largely dominated by capacity in electricity for grid usage. The Department of Energy released statistics on electricity storage, about 25 GW, in United States is comprised 94% of hydroelectric energy storage and 3% grid-battery storage. [1–4] However, the stationary nature of these energy storage method simply does not coincide with the demand of portable electronics. Since the 1980s, Nickel based portable battery with NiCd or NiMH were largely replaced by the current Li-ion battery by the 2000s. [5–9] As the portable device such as phones, laptops, and electric vehicles continues to increase their functionality and computational power, so is the demand for higher energy density battery. And this trend will continue as seen by the specific energy of lithium-ion battery over the last decade. Thus, the continuation to improve portable battery is at the heart of this progress, largely due to lithium-ion battery having more specific energy than other existing batteries (Figure 1.1).

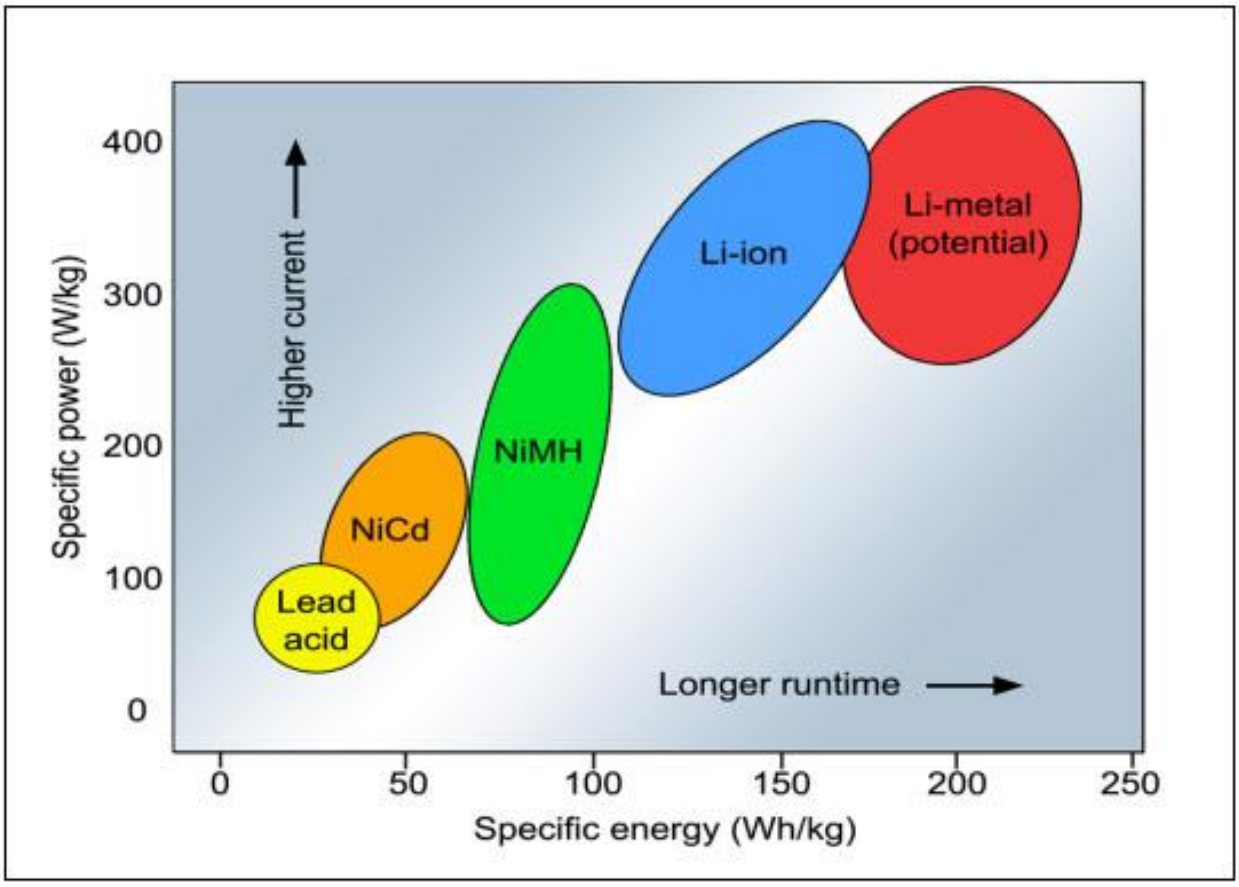

Figure 1.32. The figure shows the trend of existing batteries as specific power in W/kg versus specific energy in W h/kg [9].

The modern portable battery, largely comprised of Li-ion cell, has been in service for several decades. The cell is comprised of four components, the anode, the cathode, the electrolytes, and sometimes the separator. Each component serves a purpose in the compact design of the cell where the potential is stored in the redox reaction between the active materials in the cathode and anode. That potential is presented as cell voltage according to the following equation (1), which drives the electrons in a circuit and meet the demand of the load.

$$\mathbf{E^o_{cell} = E^o_{red} - E^o_{ox}} \qquad (1)$$

The E^{o}_{cell} represents the potential difference between the cathode and anode. The E^{o}_{red} represents the potential of the reduction reaction or the reaction at the cathode during discharge. The E^{o}_{ox} is the potential of the oxidation reaction or the reaction at the anode during discharge.

The design structure of the battery involves the cathode layer and anode layer sandwiching the electrolyte and the separator, which is typically a porous material soaked in the electrolyte. The cathode and anode materials are coated on the current collector, typically aluminum or copper.[8,10–14] When the cell is connected to a circuit the active material loses electrons and ions. The electrons paired with the potential provided by the cell is used to drive the process of the circuit, while the ions are shuttled through the electrolyte from anode to cathode. This is done to maintain charge balance in the circuit; therefore, it is paramount that the separator and the electrolyte's functionalities to remain stable through extreme conditions such as extreme high/low temperature or having large dendrite growth.

1.2 Electrolytes in Batteries

The state-of-the-art electrolytes can be categorized into three separate class, regardless of the energy storage systems that they are in. There are the organic electrolytes, inorganic electrolytes, and composite electrolytes.[15–18] These electrolytes are mostly in the form of liquids or solids, and even liquified gas in some instance demonstrated by Shirley Meng's group at UCSB.[19] Here we will look at the state-of-the-art electrolytes, their strengths and weaknesses, and their outlook.

The liquid organic electrolytes consist of ionic liquids or organic liquids capable of dissolving ion salt. The liquid organic electrolytes are the more adopted material for current Li-ion battery due to the exceptionally high ion conductivity of 10^{-3} S/cm to 10^{-2} S/cm in liquid

form, which allows for a fast ion transport between the cathode and anode.[20,21] The facile transport of ions between electrodes enables the fast charging/discharging of the cell, which is a desirable trait in the electric vehicle being able to be charged in a short period of time.[22–24] Though the organic liquid electrolyte is excellent for the current Li-ion battery, its existence in the cell hinders the adaptation of higher specific capacity material of Li metal (3840 mA h g^{-1}) and silicon anode (4200 mA h g^{-1}), due to the lack of suppression to dendrite growth on the anode. These dendrite growths, in mild severity, can lead to capacity fade over time as parts of the dendrite detach from the bulk material. And in the severe case, can penetrate the separator and lead to short of the cell or even light the already flammable organic liquid electrolyte. It is due to the need for higher energy density battery and inability of using materials such as Li metal and silicon anode that there is an increasing interest for both academia and industry to explore alternative materials to replace the existing organic liquid electrolytes in Li-ion battery.

A potential alternative replacement for organic liquid electrolyte is the organic solid electrolyte.[17,18] The organic solid electrolytes consist mostly of solid polymer material capable of dissolving common Li ion salts, such as lithium perchlorate ($LiClO_4$), lithium hexafluorophosphate ($LiPF_6$), or lithium bis(trifluoromethanesulfonyl)imide (LiTFSI). These solid polymers include materials such as polyethylene oxide (PEO), polyvinylidene fluoride (PVDF), or polyvinylpyrrolidone (PVP). These solid polymer electrolytes have a wide range of modulus for resisting the lithium dendrite growth caused pressure build up. The pressure from the dendrite growth can approach 1 to 10 GPa in some instances.[25,26] The typical modulus of the polymer ranges between 100 to 1000 MPa, which offers sufficient dendrite suppression compared to the 100 MPa offered by polyethylene (PE) separators in conventional Li-ion battery.[27,28] Though the organic polymer electrolyte offers better dendrite suppression, the ionic

conductivity of these electrolytes is typically within 10^{-4} S/cm to 10^{-6} S/cm. This range of ionic conductivity is low compared the requirement of 10^{-3} S/cm in industrial application,[17,18,21] and low compared to the liquid counterpart with ionic conductivity of 10^{-3} S/cm to 10^{-2} S/cm as well. This results in the battery require elevated temperature to reach the 10^{-3} S/cm threshold for operation. The additional issue when it comes to salts being dissolved in these organic electrolytes is the theoretical limitation to the transference number. The transference number accounts for the percent of ions shuttled across the electrolyte during charge/discharge being the active ions, such as the lithium ion in Li-ion battery. However, because a salt is dissolved in the electrolyte, the transference number is cut in half to 0.5 theoretically, which presents itself as utilizing only half of the measured ionic conductivity. Many publications attempt to address the problem of low ionic conductivity and low transference number of solid polymer electrolyte by immobilizing ionic liquids in polymer matrix to make ion gels, or by bonding functional groups with the polymer to make single ion conductors.[29–32] These electrolytes have typical ionic conductivity up to 10^{-4} S/cm and transference number close to 0.9 in some cases.

While the solid organic polymer electrolytes are approaching the required 10^{-3} S/cm ionic conductivity, the inorganic solid electrolyte has the highest ionic conductivity in comparison to the rest of solid electrolytes.[33–35] The inorganic solid electrolytes are typically composed of crystalline structures with phosphates, oxides, sulfides, hydrides, nitrides, and halides, while ion conduction rely on point defects and ion hopping mechanism to shuttle Li ion between the cathode and anode. Common example of these inorganic solid electrolytes consists of lithium germanium phosphorus sulfides (LGPS), lithium lanthanum titanate (LLTO), lithium lanthanum zirconium oxide (LLZO), or lithium phosphorus oxynitride (LiPON). These inorganic crystalline electrolytes typically require binder material such as PVDF to hold a free-standing

film with impressive ionic conductivity of 10^{-4} S/cm to 10^{-3} S/cm, all the while maintaining a high transference number of 0.99 in many cases. This is not to say that these crystalline electrolytes must have polymer electrolytes as binder to operate. In certain cases, using unconventional growth techniques, such as PVD/CVD or dip-coating and annealing, research groups have been able to grow entire battery with the cathode, anode, and solid electrolyte instead of preparing separate components and then sandwiching them together in a press.[36] The grown crystalline halide has shown remarkable ionic conductivity of 10^{-2} S/cm. Going back to the common crystalline electrolytes percolating within a polymer matrix, they suffer from low voltage window due to usage of polymer electrolyte binder and contain grain boundaries that reduces the bulk ionic conductivity of these material.

1.3 Important Properties for Electrolytes

When considering usage of electrolytes in batteries, there are several key parameters measured for comparison. These includes, ionic conductivity, ion mobility, transference number, voltage window, cyclability, Young's modulus, electrode compatibility, activation energy, and thermal resistance. All these factors should be considered when selecting electrolytes, however, most of the focus in most publications are the ionic conductivity, activation energy, and transference number of the electrolyte material.

The ionic conductivity is of chief importance because of the functionality of the electrolyte, which is to conduct ions between the electrodes. The flow of charged particle ($\Delta\mathbf{q}$) over time ($\Delta\mathbf{t}$) is the current (**I**) (eq 1) and the conducting ions under a voltage (**V**) is subjected to resistance (**R**) (eq 2), just like Ohm's law is obeyed for electrons flowing across a conductive material when a potential is applied.

$$\frac{\Delta q}{\Delta t} = I \quad (1)$$

$$V = I \cdot R \quad (2)$$

And the inverse of resistance can be taken to be the conductance (**G**) (eq 3), and with inclusion of dimensionality such as cross-sectional area (**A**) and length (l), resistivity **(ρ**) is obtained (eq 4).

$$G = \frac{1}{R} \quad (3)$$

$$\rho = R\frac{A}{l} \quad (4)$$

Resistivity is a fundamental property on the measured material to resists the movement of charged particles, such as electrons or ions. Resistivity can be related to conductivity by the same inverse relationship between resistance and conductance, and thus ionic conductivity of a material can be clearly defined (eq 5).

$$\sigma = \frac{1}{\rho} = \frac{l}{RA} \quad (5)$$

Knowing the ionic conductivity can be measured, with units in Siemens per centimeter (S/cm), allows for comparison of the ability for different solid-state electrolytes to conduct electrons and ions. However, due to the solid electrolytes made of mainly oxides, sulfides and polymers, the electronic conductivity is often several orders of magnitude smaller when

compared to ionic conductivity, they are electronically insulating. When it comes to measurement of ionic conductivity, constant voltage is not used to measure the resistance of the material. Because unlike electrons, the ions displacement is a slower process and prone to polarization of the cell, thus leading to inconsistency in the measured resistance depending on the duration that the cell is subjected to the constant voltage.

To address this, resistance for solid state electrolytes is measured using Electrochemical Impedance Spectroscopy (EIS). EIS perturbs the system or material with a small (typically between 10 mV to 100 mV) and oscillating voltage, thus making EIS a non-destructive measurement process as the voltage across the system is oscillating between positive and negative set magnitude. When the perturbing voltage is applied and the current is measured, just like Ohm's law, there is a dependency between the perturbing voltage (V(t)), measured current (I(t)) and impedance (Z). The impedance is measured in units of Ω (eq 6).

$$\boldsymbol{V(t) = Z \cdot I(t)} \tag{6}$$

The measured time dependent current can provide information on the impedance when paired with the perturbing voltage at a specific frequency. The perturbing voltage (eq 7) is applied across a wide range of frequency, typically ranging from 1 MHz to 1 Hz. And thus, the applied voltage displaces charged particles, and generates a lagging current that is measured with a phase shift constant $\boldsymbol{\phi}$. (eq 8)

$$\boldsymbol{V(t) = V_o \sin(\omega t)} \tag{7}$$

$$\boldsymbol{I(t) = I_o \sin(\omega t + \phi)} \tag{8}$$

And with a wide range of frequency for applied voltage, displacement of different charged particles and reaction process can be resolved in the impedance value. For instance, when scanning from the beginning high frequency of 1 MHz, the primary displaced charged particles are electrons. Heavier ions such as H_3O^+, Li^+, and Na^+ do not respond to the high frequency voltage applied to them, thus registering only the electronic resistance of the material. However, as frequency of the perturbing voltage decrease, the time frame of the larger ions being subjected to the voltage is increased, and they respond to the stimulus by vibrating and creating the lagging current. So, by analyzing the different impedance value across a range of frequency, information can be obtained about the resistance value of a specific process, such as ion transport.

In typical ionic conductivity measurement using EIS, the measured impedance is plotted on a Nyquist plot for ease of analysis. Due to the sinusoidal nature of eq 7 and eq 8, the relationship can be applied to Euler's formula (eq 9) on the perturbing voltage and measured current. And combining V(t) and I(t) together, the impedance (Z) can be calculated.

$$e^{ix} = \cos(x) + i\sin(x) \tag{9}$$

$$V(t) = V_o e^{iwt} \tag{10}$$

$$I(t) = I_o e^{iwt-\phi} \tag{11}$$

$$\frac{V(t)}{I(t)} = Z_o e^{i\phi} = Z_o(cos(\phi) + i\,sin(\phi)) \tag{12}$$

From the combined equation 12, the measured impedance can be projected on a real and imaginary impedance space as an impedance vector |Z| with the angle from the real axis being the phase shift constant ϕ. Note that the impedance value in Eq 12 has a real component and an imaginary component, which can be represented on the Cartesian coordinate as a vector |Z|. This is illustrated below with vector |Z|.

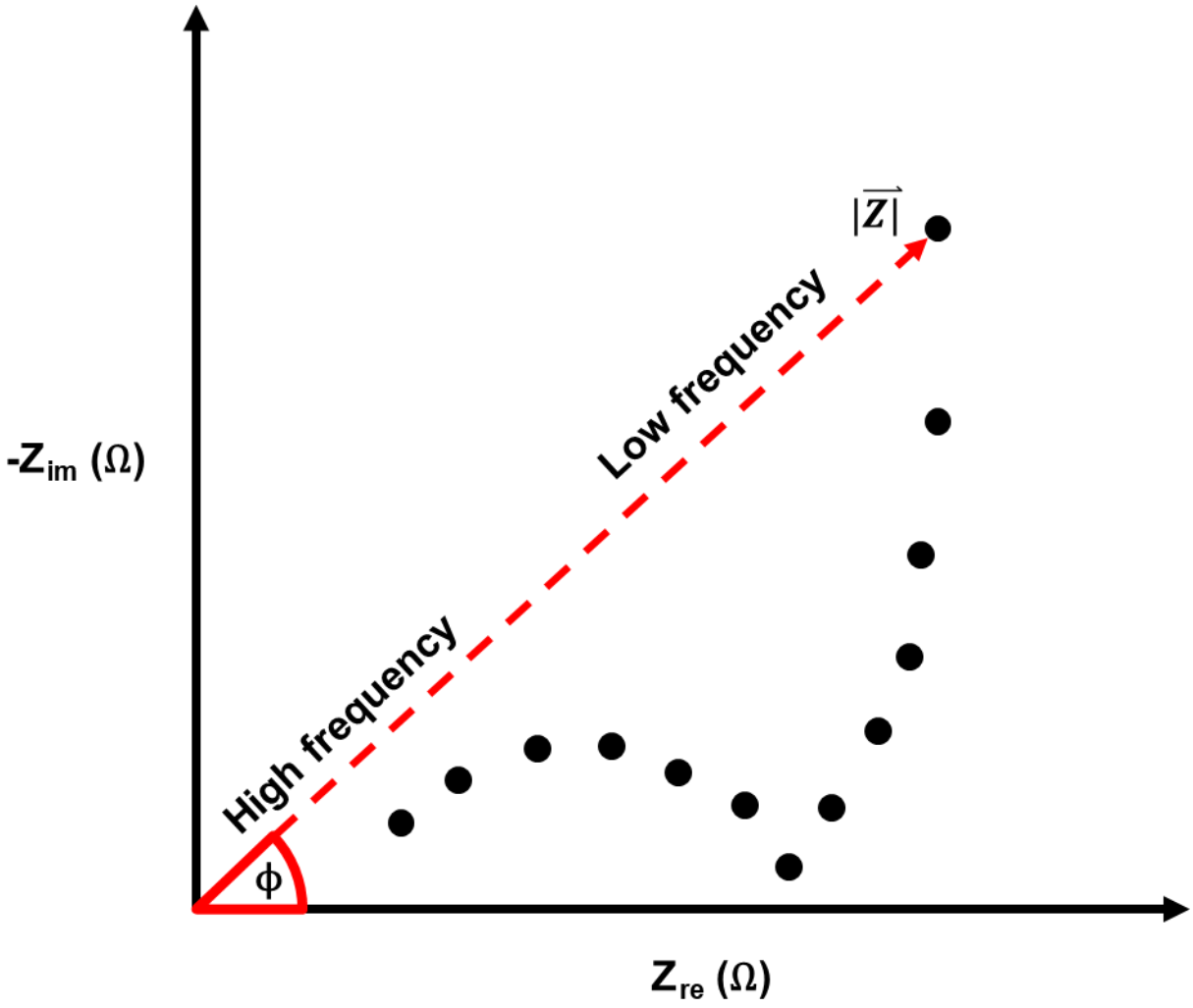

Figure 1.33. Figure demonstrates the Nyquist plot with x-axis being real impedance (Z_{re}) and y-axis being negative imaginary impedance ($-Z_{im}$). The dots represent each impedance

vector |Z| measured at different frequency, starting with impedance measured at the highest frequency going towards lower frequencies.

Once the data is collected, equivalent circuit fitting can be used to simulate a similar curve which follows the data points, the fitted equivalent circuit can then provide information on the resistance value of the circuit elements (Figure 1.2). Note that this method is a way of estimating the value of resistance for a simple setup and require reproducibility of the Nyquist plot. For instance,

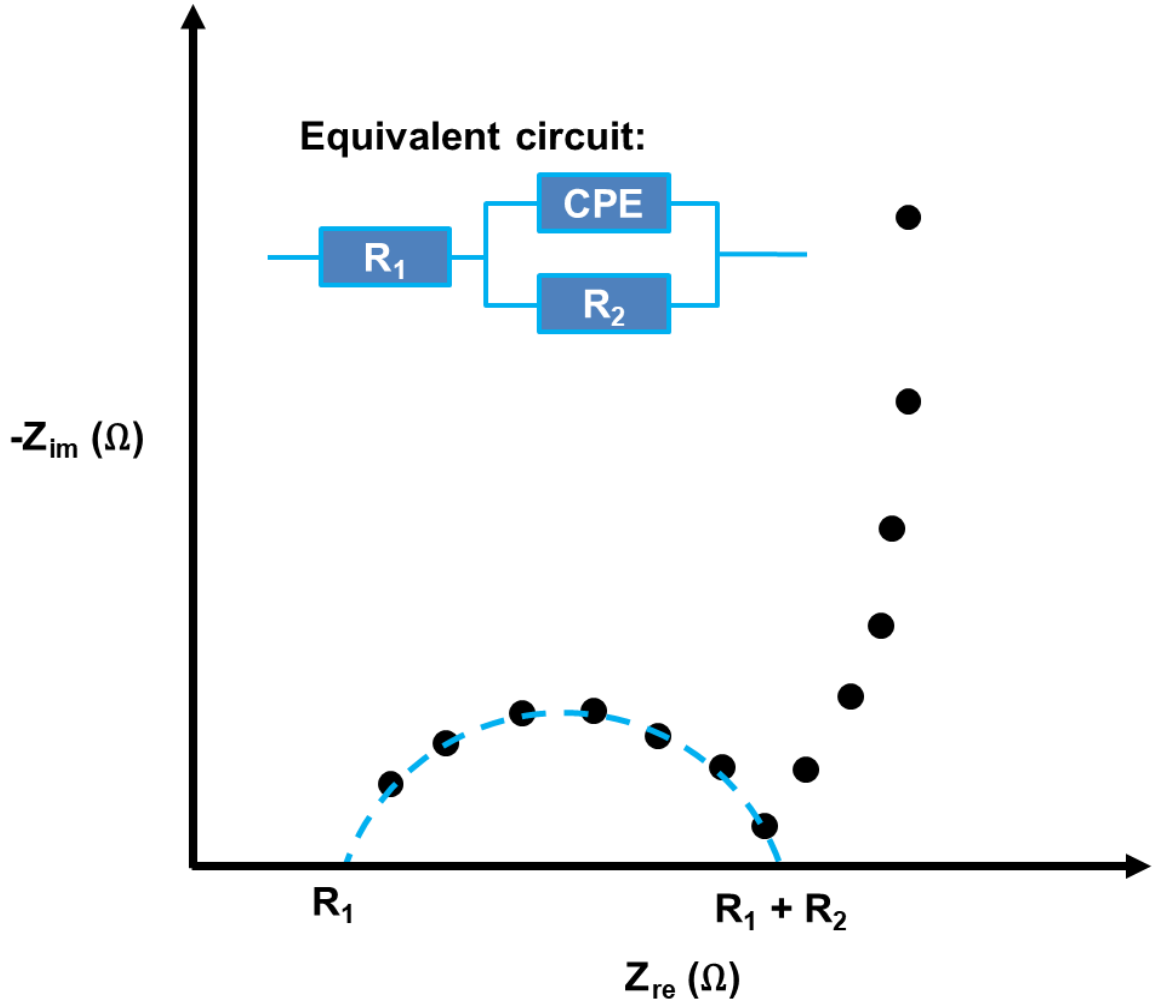

Figure 1.34. The figure demonstrates the analysis of collected data on Nyquist plot, the inset represents a fitted equivalent circuit, which simulates the dotted blue line with the diameter of the semicircle being R_2. The equivalent circuit is comprised of a series resistor (R_1) connected to a constant phase element (CPE) in parallel to a second resistor (R_2).

Due to the measurement process being frequency dependent, and different conductivity and reactions register their impedance at different frequency ranges, a complex system will make the measurement process difficult (Figure 1.3). For instance, a solid-state electrolyte that contains two separate electrochemical process may show two separate semicircles on the Nyquist plot.

The equivalent circuit fitting can be used to estimate the magnitude of the resistance for each of the semicircle, however it does not tell which electrochemical process they are associated to. To address this, the user of EIS can attempt to manipulate the resistance value of one of the electrochemical process. However, this can be unreliable as different electrochemical process in the same system are often coupled. One can also utilize the frequency dependency of the electrochemical process for identification, which is related to analysis of Bode plots. So typical measurement of ionic conductivity or electrochemical process are on simple systems, such as a symmetrical cell with the material sandwiched between two stainless steel plates (SS) or blocking electrodes (Figure 1.4 a,b). Blocking electrodes, are electrodes that do not participate in the electrochemical process of interest, they are there simply to complete the circuit. In this setup, only the electronic and ionic resistance are measured shown in the figure below.

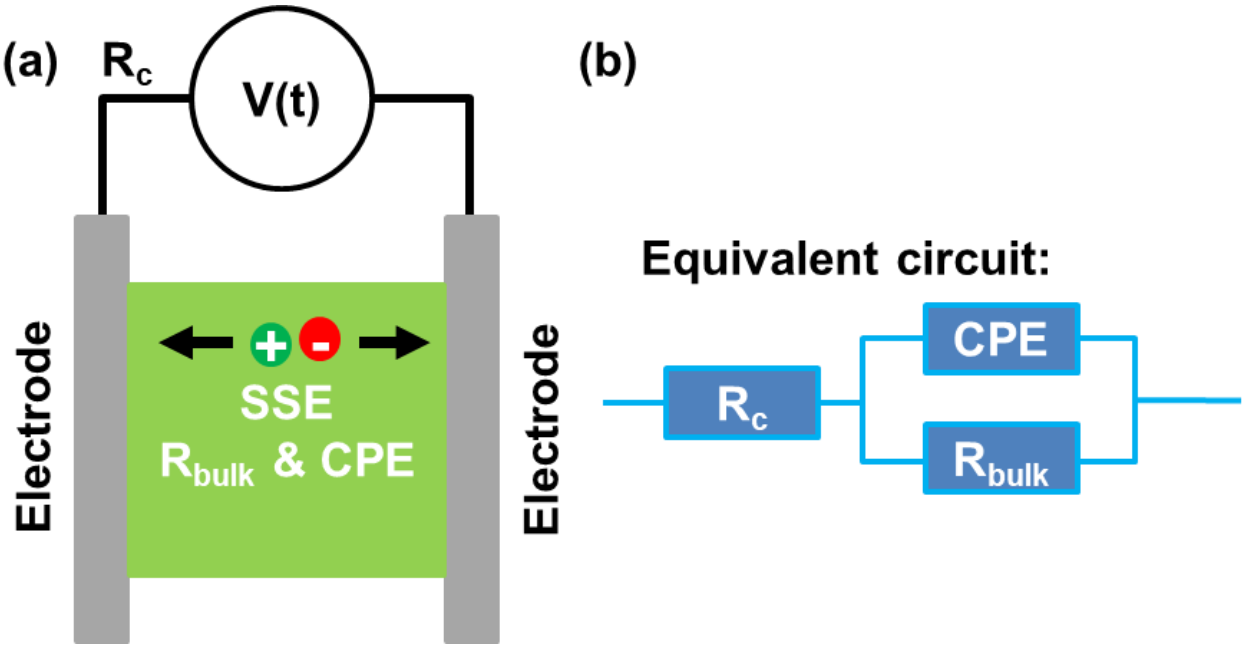

Figure 1.35. The figure (a) shows the setup for a simple symmetric cell with SS/electrolyte/SS configuration, cations and anions are depicted as dark green and red dot. The symmetric cell is connected to a sinusoidal voltage V(t). The setup includes the circuit

resistance (R_c) and ionic resistance (R_{bulk}). (b) The equivalent circuit fitting is a simplified Randle's circuit with the R_c in series to the parallel CPE and R_{bulk}.

EIS provides one additional piece of information when examining the electrochemical process, and it is the frequency dependence of the process, typically represented in Bode plots. Which can sometimes provide information on separating the identity of the semicircles, if it is reproducible and there is a large enough separation of the frequency. The Bode plot shows the phase shift element ϕ against frequency. This shows the frequency when the resistance value is in the real space or when ϕ is equal to 0 degree. In other words, it identifies the frequency at which the electrochemical process is in action, allowing for identification of the process.

Due to the non-destructive nature of the EIS during testing, EIS can be paired with other equipment to provide additional information about the material being studied. For instance, pairing EIS with a temperature control stage can be used to measure activation energy. The activation energy (E_a) can be calculated from Arrhenius relationship between temperature and ionic conductivity (σ) of the material. Note this only considers ionic conductivity from the EIS measurement in the below equation (eq 13), with the coefficient (A), Boltzmann's constant (k_β), and measurement temperature (T).

$$\boldsymbol{\sigma = A\, e^{-\frac{E_a}{k_\beta T}}} \tag{13}$$

$$\boldsymbol{-\log(\sigma) = \frac{E_a}{k_\beta T} - \log(A)} \tag{14}$$

Treating both sides of the eq 13 with – log, we see a linear relationship between -log(σ) and 1/T, making E_a/ k_β as the slope of the curve, which can be calculated if the slope of the curve is measured. For instance, in the figure below,

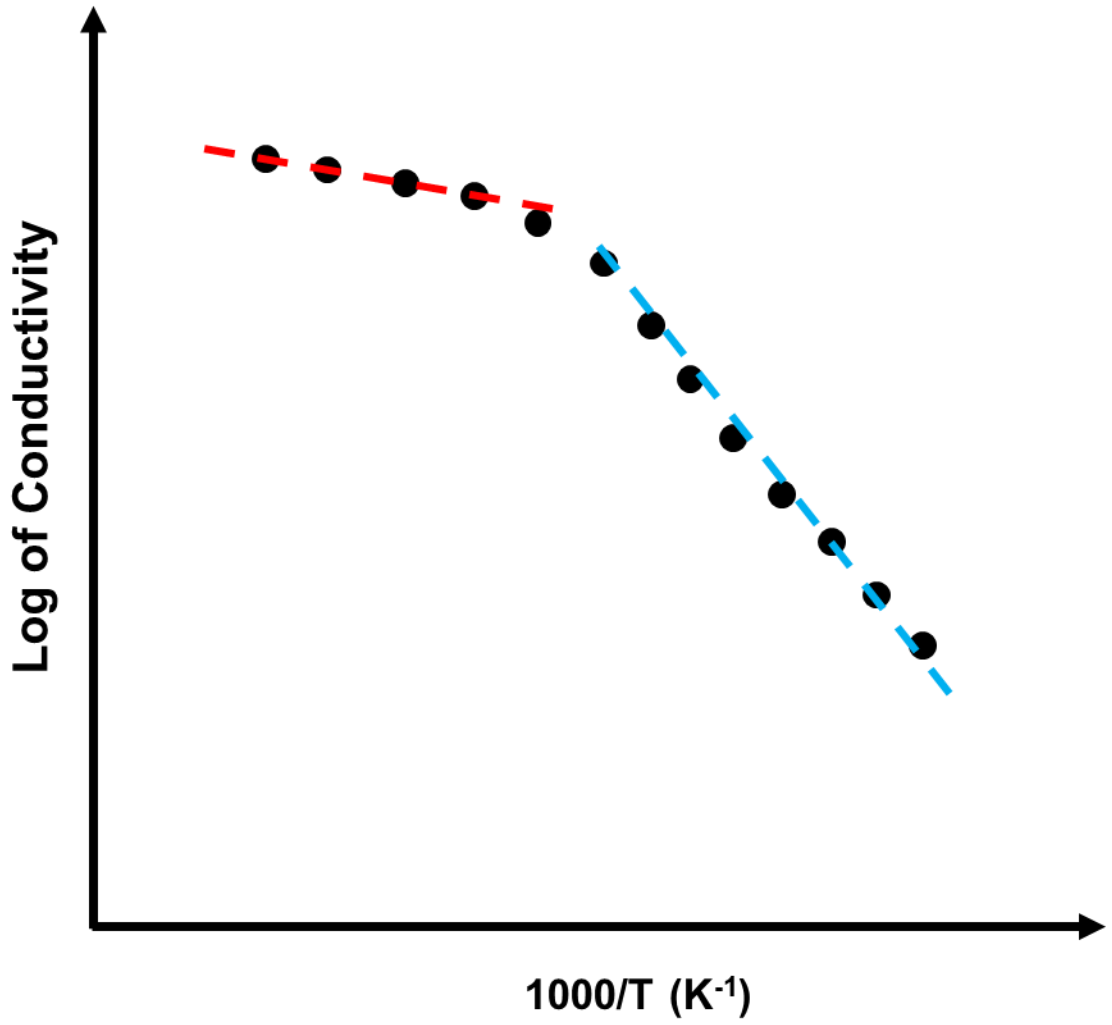

Figure 1.36. The figure depicts the measurement of ionic conductivity versus temperature, the data points are the black dots. The red and blue dotted line shows the slope of the two curves that appear from the measurement.

From the figure, the activation energy of the ionic conducting process can be calculated and compared (Figure 1.5). Not only does the Arrhenius relationship allow for measurement of activation energy, but it also provides insight to the behavior of ion conduction under various electrolyte environment. In figure 4, we see the existence of two separate slope, which indicates a change in the ion conduction mechanism. To be more specific, there is a change in the environment surrounding the ion conduction pathway, which leads to either more or less activation energy required to move the ions. Typically, the change in activation energy is a sign of phase change or morphological change in the hosting material for the ions. Furthermore, the Arrhenius plot also allows for observation of the thermal degradation to the electrochemical process, by scanning the ionic conductivity in reverse sweep. If the thermal degradation does not happen or does not affect the ion transport mechanism, then the reverse sweep should provide the same slope during the reverse sweep, meaning the process is reversible. And if the reverse sweep shows increase magnitude in slope, it is a good indication that an irreversible thermal degradation has happened. With this, the material's performance under thermal degradation can be measured and compared to other materials.

Lastly, when it comes to EIS providing information on the ionic conductivity of the material. It does not resolve different conduction process and electrochemical process, for instance, the cation transport and anion transport. Due to the similar mechanism that the cation and anion conduct through, it is difficult to discern only cation conduction or only anion conduction with EIS alone. But pairing EIS with single potential amperometry, a coefficient that describes the percent of cation transport in the total ionic conductivity can be obtained, also known as transference number ($\mathbf{t}^{+}$). In the simplest estimation of transference number, a constant voltage can be applied across a symmetrical cell with active electrodes, which are electrodes that

do participate in the electrochemical process and completes the circuit. The simple estimation follows the equation below,

$$t^{+} = \frac{I_{\infty}}{I_{o}} \tag{15}$$

To measure the transference number for lithium cation conduction in a solid-state electrolyte, a symmetrical cell with Li/electrolyte/Li configuration is made. A constant voltage is applied for several hours, the initial current (I_o) and the steady-state current (I_∞) are used to estimate the transference number. Because when the initial voltage is applied to this cell setup, both cation and anions are being conducted across the electrolyte, which provides a higher initial current. At this point, both the cation and anion are contributing to the overall current. Then, as the constant voltage continue to be applied, the anion in the electrolyte is depleted and pressed towards the cathode. While the lithium cation in this case is transported towards the anode, but due to the electrodes being active electrodes, Li, there is a steady supply of lithium ion being transported across the electrolyte. Overtime, the measured current will decrease and plateau, reaching a steady state because the anion is depleted and only lithium cation is transported across.

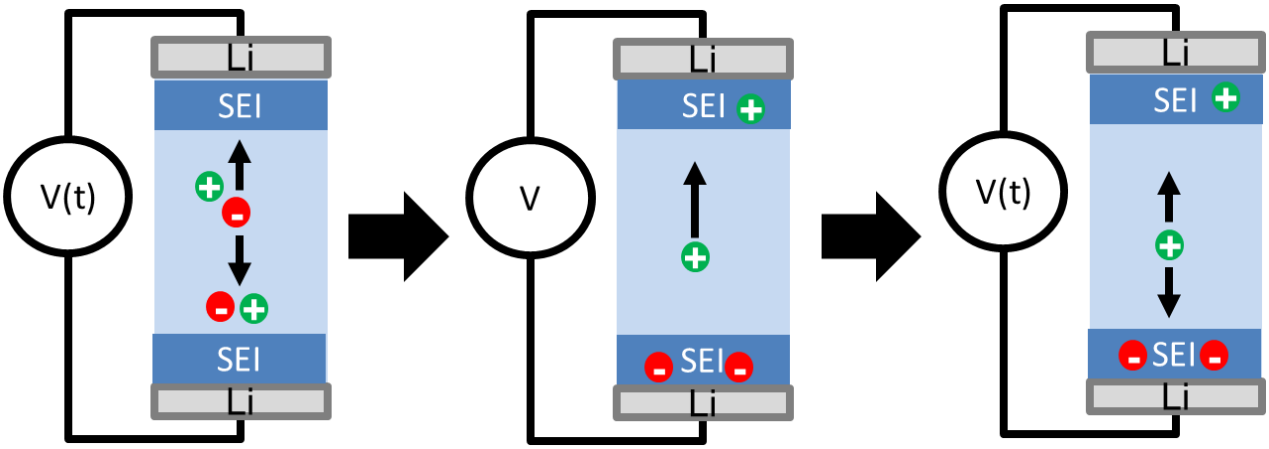

Figure 1.37. The left panel shows the initial state of the potentiostatic polarization measurement, where EIS is used to measure the initial resistance R_o. The middle panel shows the constant voltage applied to the cell which measures initial current I_o and steady state current I_∞. The right panel shows the final state of the measurement, where the steady state resistance R_∞ is measured.

However, this approximation of the transference number is over simplified. Side electrochemical reaction can take place within the cell, such as solid electrolyte interface (SEI). The formation of SEI is primarily due to the reduction potential of lithium among the lowest, at E^o = -3.04 V. Which according to Gibbs free energy (ΔG^o), eq 17, it would be a spontaneous process for lithium metal to reduce most material that is in contact with it, provided that the overall reaction is still spontaneous according the eq 17.

$$Li^+ + e^- \rightarrow Li_{(s)}, \qquad E^o = -3.04\,V \tag{16}$$

$$\Delta G^o = -nFE^o_{cell} \tag{17}$$

Thus, as the initial SEI layer is formed during the constant voltage applied across the symmetrical cell with active electrodes, the SEI will continuously grow for the duration of the test. This leads to the problem of current lost and the increase in the resistance contributed by the growth of SEI. Therefore, the simplified transference number equation does not adequately represent the cation contribution to the overall ionic conductivity (Figure 1.6). To address this, eq 18 is adopted.

$$t^{+} = \frac{I_{\infty}(V - I_o R_o)}{I_o(V - I_{\infty} R_{\infty})} \tag{18}$$

This equation is derived by James Evans, Colin A. Vincent, and Peter G. Bruce, which provides a reasonable adjustment to the growth of the passivating layer. By using EIS to measure the initial and steady state resistance, and potentiostatic polarization method to measure the initial and steady state current when a voltage is applied.

Using the transference number from the potentiostatic polarization method and the ionic conductivity value from EIS, the contribution of cation to the overall ionic conductivity can be presented and compared to between materials. This is a meaningful value to present, due to most of battery systems relying only on one type of ions to operate. Knowing how much of the ionic conductivity is due to the ion of interest can provide further insight to the ion conduction mechanism to be further improve the capability of solid-state electrolyte in batteries.

1.4 References

1. Albertus, P., Manser, J. S. & Litzelman, S. Long-Duration Electricity Storage Applications, Economics, and Technologies. *Joule* **4**, 21–32 (2020).

2. Yang, Z., Liu, J., Baskaran, S., Imhoff, C. H. & Holladay, J. D. Enabling renewable energy-and the future grid-with advanced electricity storage. *Jom* **62**, 14–23 (2010).

3. Abbas A. Akhil, Georgianne Huff, Aileen B. Currier, Benjamin C. Kaun, D. M. R. & Stella Bingqing Chen, Andrew L. Cotter, Dale T. Bradshaw, and W. D. G. DOE/EPRI 2013 Electricity Storage Handbook in Collaboration with NRECA. (2013).

4. Electricity Storage | Energy and the Environment | US EPA. Available at: https://www.epa.gov/energy/electricity-storage. (Accessed: 23rd June 2021)

5. Köhler, U., Kümpers, J. & Ullrich, M. High performance nickel-metal hydride and lithium-ion batteries. *J. Power Sources* **105**, 139–144 (2002).

6. Jung, D. Y., Lee, B. H. & Kim, S. W. Development of battery management system for nickel-metal hydride batteries in electric vehicle applications. *J. Power Sources* **109**, 1–10 (2002).

7. Müller, T. & Friedrich, B. Development of a recycling process for nickel-metal hydride batteries. *J. Power Sources* **158**, 1498–1509 (2006).

8. Reddy, M. V., Mauger, A., Julien, C. M., Paolella, A. & Zaghib, K. Brief history of early lithium-battery development. *Materials (Basel).* **13**, 1–9 (2020).

9. BU-103: Global Battery Markets - Battery University. Available at: https://batteryuniversity.com/article/bu-103-global-battery-markets. (Accessed: 23rd June 2021)

10. Masaki Yoshio, H. N. *Lithium-Ion Batteries, Chapter 2*. *Lithium-Ion Batteries* (2009).

11. Obrovac, M. N., Christensen, L., Le, D. B. & Dahn, J. R. Alloy Design for Lithium-Ion

Battery Anodes. *J. Electrochem. Soc.* **154**, A849 (2007).

12. Liu, K., Liu, Y., Lin, D., Pei, A. & Cui, Y. Materials for lithium-ion battery safety. *Sci. Adv.* **4**, (2018).

13. BU-104b: Battery Building Blocks - Battery University. Available at: https://batteryuniversity.com/article/bu-104b-battery-building-blocks. (Accessed: 23rd June 2021)

14. BU-205: Types of Lithium-ion - Battery University. Available at: https://batteryuniversity.com/article/bu-205-types-of-lithium-ion. (Accessed: 23rd June 2021)

15. Zhang, S. S. Liquid electrolyte lithium/sulfur battery: Fundamental chemistry, problems, and solutions. *J. Power Sources* **231**, 153–162 (2013).

16. Abouimrane, A., Ding, J. & Davidson, I. J. Liquid electrolyte based on lithium bis-fluorosulfonyl imide salt: Aluminum corrosion studies and lithium ion battery investigations. *J. Power Sources* **189**, 693–696 (2009).

17. Zheng, F., Kotobuki, M., Song, S., Lai, M. O. & Lu, L. Review on solid electrolytes for all-solid-state lithium-ion batteries. *J. Power Sources* **389**, 198–213 (2018).

18. Ma, Q. & Tietz, F. Solid-State Electrolyte Materials for Sodium Batteries: Towards Practical Applications. *ChemElectroChem* **7**, 2693–2713 (2020).

19. Rustomji, C. S. *et al.* Liquefied gas electrolytes for electrochemical energy storage devices. *Science (80-.).* **356**, (2017).

20. Francis, C. F. J., Kyratzis, I. L. & Best, A. S. Lithium-Ion Battery Separators for Ionic-

Liquid Electrolytes: A Review. *Adv. Mater.* **32**, 1–22 (2020).

21. Quartarone, E. & Mustarelli, P. Review—Emerging Trends in the Design of Electrolytes for Lithium and Post-Lithium Batteries. *J. Electrochem. Soc.* **167**, 050508 (2020).

22. Erdinc, O. Economic impacts of small-scale own generating and storage units, and electric vehicles under different demand response strategies for smart households. *Appl. Energy* **126**, 142–150 (2014).

23. QuantumScape building electric car battery that charges to 80% in 15 minutes. Available at: https://www.cnbc.com/2020/12/08/quantumscape-building-electric-car-battery-that-charges-to-80percent-in-15-minutes.html. (Accessed: 23rd June 2021)

24. Presentations & Videos - QuantumScape. Available at: https://www.quantumscape.com/technology/presentations-videos/. (Accessed: 23rd June 2021)

25. Barai, P., Higa, K. & Srinivasan, V. Lithium dendrite growth mechanisms in polymer electrolytes and prevention strategies. *Phys. Chem. Chem. Phys.* **19**, 20493–20505 (2017).

26. Liu, G. & Lu, W. A Model of Concurrent Lithium Dendrite Growth, SEI Growth, SEI Penetration and Regrowth. *J. Electrochem. Soc.* **164**, A1826–A1833 (2017).

27. Patel, A. *et al.* High Modulus, Thermally Stable, and Self-Extinguishing Aramid Nanofiber Separators. *ACS Appl. Mater. Interfaces* **12**, 25756–25766 (2020).

28. Kalnaus, S., Wang, Y. & Turner, J. A. Mechanical behavior and failure mechanisms of Li-ion battery separators. *J. Power Sources* **348**, 255–263 (2017).

29. Li, H. *et al.* A novel single-ion conductor gel polymer electrolyte prepared by co-

irradiation grafting and electrospinning process. *Solid State Ionics* **347**, 115246 (2020).

30. Pan, Q. *et al.* A dense transparent polymeric single ion conductor for lithium ion batteries with remarkable long-term stability. *J. Power Sources* **336**, 75–82 (2016).

31. Choi, N. S., Lee, Y. M., Lee, B. H., Lee, J. A. & Park, J. K. Nanocomposite single ion conductor based on organic-inorganic hybrid. *Solid State Ionics* **167**, 293–299 (2004).

32. Seino, Y., Ota, T., Takada, K., Hayashi, A. & Tatsumisago, M. A sulphide lithium super ion conductor is superior to liquid ion conductors for use in rechargeable batteries. *Energy Environ. Sci.* **7**, 627–631 (2014).

33. Liu, Q. *et al.* Challenges and perspectives of garnet solid electrolytes for all solid-state lithium batteries. *J. Power Sources* **389**, 120–134 (2018).

34. Cheng, L. *et al.* Effect of surface microstructure on electrochemical performance of garnet solid electrolytes. *ACS Appl. Mater. Interfaces* **7**, 2073–2081 (2015).

35. Shin, B. R. *et al.* Comparative study of TiS2/Li-In all-solid-state lithium batteries using glass-ceramic Li3PS4and Li10GeP2S12 solid electrolytes. *Electrochim. Acta* **146**, 395–402 (2014).

36. Chi, X. *et al.* A highly stable and flexible zeolite electrolyte solid-state Li–air battery. *Nature* **592**, 551–557 (2021).

Chapter 2. Application of Percolation Pathway in Solid Polymer Electrolyte for Efficient Ion Transport Mechanism

2.1 Introduction

Energy storage devices such as battery has largely been dominated by lithium-ion batteries over the past two decades.[1–4] However, with the increase in complexity of devices operating on lithium-ion battery, the energy density requirement for these devices has also increased overtime. The lithium-ion battery being the dominant energy storage option for mobile power supply is reaching its limitation. Novel methods to increase energy density and charge/discharge speed of the battery for existing lithium-ion battery technology is paramount to addressing the further development of more complex devices, such as the mobile phones or electric vehicles. To address the requirement of fast charge and discharge,[5–7] the ionic conductivity and ability to establish large surface area of contact with porous electrodes for the electrolyte system takes the center stage.

Existing electrolyte in lithium-ion battery technology is comprised of primarily a porous polymer separator, typically polyethylene (PE), soaked in organic solvent, such as a mixture of diethyl carbonate (DEC), dimethyl carbonate (DMC), or ethylene carbonate (EC) with lithium salt source, LiTFSI, $LiClO_4$, and $LiPF_6$ acting as the Li^+ when dissolved.[8,9] The solvated Li^+ can then be shuttle across the interface towards cathode during discharge, and towards the anode during charging. All of this happens within a thin interface supported by the porous polymer separator between the cathode and anode, with the porous membrane preventing direct contact between the electrodes. Because the transport mechanism of Li^+ in liquid solvent is a facile

process with ionic conductivity typically around 10^{-2} to 10^{-3} S/cm,[10–12] and the excellent wettability of liquid electrolyte with porous electrode materials, making alternatives to the organic solvent system unable to compete. Thus, the consideration of alternatives was largely ignored for decades. However, recent publication on gel electrolytes have demonstrated the viability of a composite system with both liquid electrolytes and polymer electrolyte.[13–18] For instance,

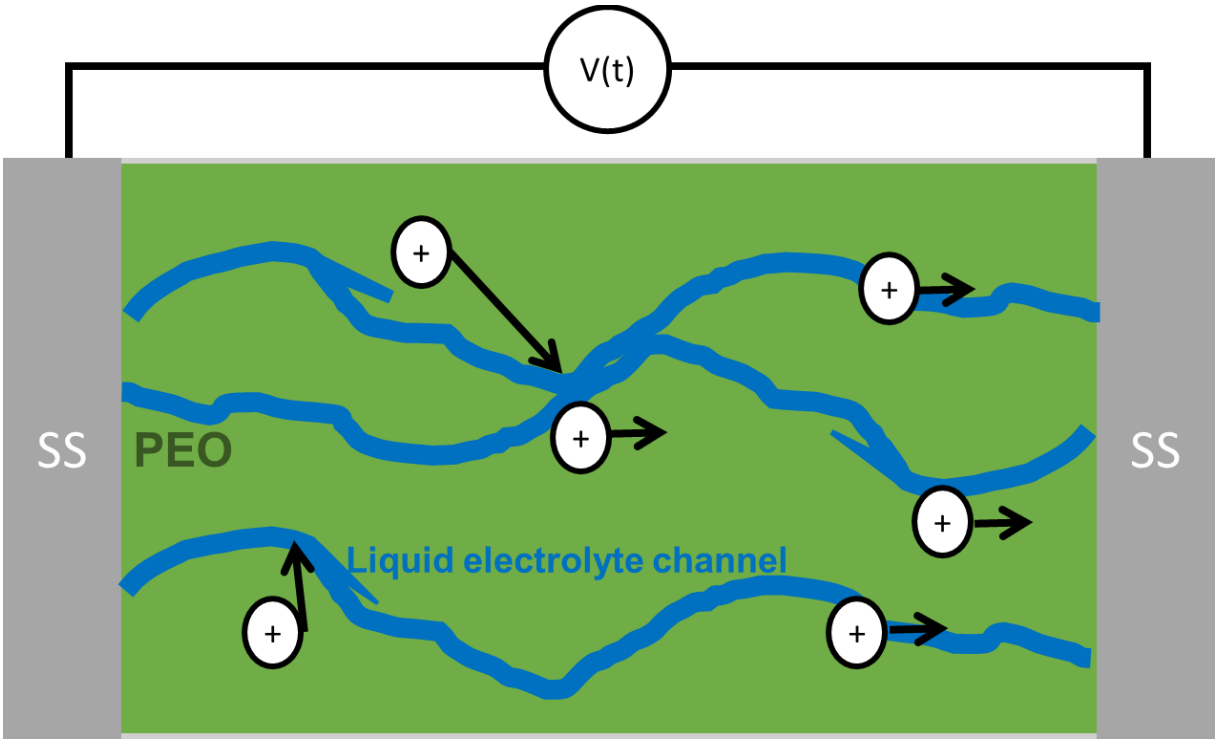

Figure 2.38. The figure demonstrates the idea of adding enough FMSN to the PEO electrolyte to create direct ion transport pathways, so that Li^+ ions can be shuttled in the liquid electrolyte channel in a facile manner, the composite solid electrolyte is sandwiched between two electrodes, such as stainless steel or Au/Ti coated glass.

Here we demonstrate attempts to create composite gel electrolyte with PEO polymer electrolyte as the matrix surrounding $LiClO_4$ and water encased functionalized mesoporous silica

nanoparticles (FMSN), which provides a facile ion transport pathway when loading of FMSN approaches 20% by volume through the percolation effect (Figure 2.1). The percolating channel of FMSN in the polymer electrolyte can utilize the liquid electrolyte stored within as facile transport channel. So, looking at the bigger picture, the Li^+ can attain the 10^{-2} and 10^{-3} S/cm ionic conductivity through the channel while the composite electrolyte still maintains the mechanical property of a solid polymer electrolyte.

2.2 Experimental

The synthesis of mesoporous silica nanoparticles (MSN) is through hydrothermal reaction of tetraethyoxy silane (TEOS) by hydrolysis and condensation reaction in the presence of micelles created by cetyl trimethyl ammonium bromide (CTAB). This process is also known as a surfactant assisted self-assembly sol gel process in a Stöber solution. Briefly, a 100 mL of distilled water is mixed with 200 mg of cetyl trimethyl ammonium bromide and 2.0 mL of a 1.0 M NaOH solution. Once the CTAB is completely dissolved and no white solids remain in solution and the solution is heated to 70^{o}C, 1.2 g of TEOS is added dropwise and the solution is stirred for 5 hours at 70^{o}C. During the 5 hours period, white precipitates begin to form and trapping the CTAB micelles within the mesoporous silica nanoparticles. Once the reaction is complete, the MSN is collected via gravity filtration and washed with distilled water, methanol, and acetone. The gravity filtered MSN paste is then vacuum dried overnight to be collected as a white solid. The dried MSN is then sintered in an annealing furnace under air condition at 500 ^{o}C to burn away the remaining cetyl trimethyl ammonium bromide surfactant. TEM images of the as made MSN were taken.

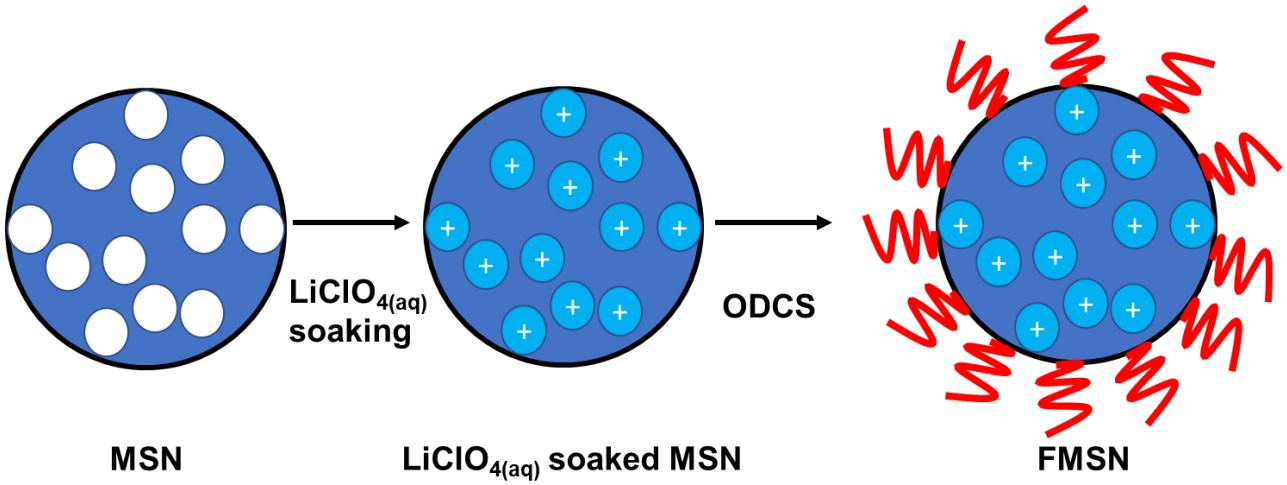

Figure 2.39. The figure shows the synthesis process of functionalized mesoporous silica nanoparticle (FMSN), starting with mesoporous silica nanoparticles (MSN), soaked in $LiCLO_{4(aq)}$ to fill the pores in the middle, and then functionalized with octadecyl trichlorosilane in hexane, to surround the surface structure of the soaked MSN with nonpolar hydrocarbon chains (red) as to encase the electrolyte solution to make the final functionalized mesoporous silica nanoparticles (FMSN).

The synthesis of $LiClO_4$ solution encased in functionalized mesoporous silica nanoparticles are performed through solvothermal synthesis methods (Figure 2.2). Briefly, the sintered mesoporous silica nanoparticles are soaked in a solution of 1.0 M $LiClO_4$ in distilled water for 1 day with stirring. The soaked MSN is then collected and dropped into a stirring solution of 2.0 M octadecyl trichlorosilane (ODCS) in 30 mL of hexane, the ODCS reacts rapidly with the surface of MSN to create a surface functionalized mesoporous silica nanoparticle (FMSN) with $LiClO_4$ electrolyte encased (Figure 2.3 a). The FMSN is then collected and dried mildly under air condition.

The polymer membrane and composite polymer membranes were made by slurry coating method. Briefly to make the polymer electrolyte, a liquid electrolyte solution of 1.0 M $LiClO_4$ in 10 mL acetonitrile was made, then 400 mg of PEO 600,000 M_w was added directly into the liquid electrolyte solution while stirring, and left stirring for 2 hours. The resulting viscous solution is then dropped on an Au/Ti deposited glass slide, as the electrode, and a doctor's blade is used to coat the surface evenly. The coated electrodes were then air dried for 1 hour before being sandwiched with another Au/Ti deposited glass slide to form a symmetrical cell with blocking electrodes. To make the composite polymer membrane, similar techniques to the process of making polymer membrane were used. First, a liquid electrolyte solution of 1.0 M $LiClO_4$ in 10 mL acetonitrile was made, then 400 mg of PEO 600,000 M_w was added directly into the liquid electrolyte solution while stirring, and left stirring for 2 hours. And then 300 mg of the MSN and FMSN can be added directly to the viscous solution while stirring. The resulting white viscous solution is then dropped on an Au/Ti deposited glass slide, as the electrode, and a doctor's blade is used to coat the surface evenly (Figure 2.3 b). The coated electrodes were then air dried for 1 hour before being sandwiched with another Au/Ti deposited glass slide to form a symmetrical cell with blocking electrodes.

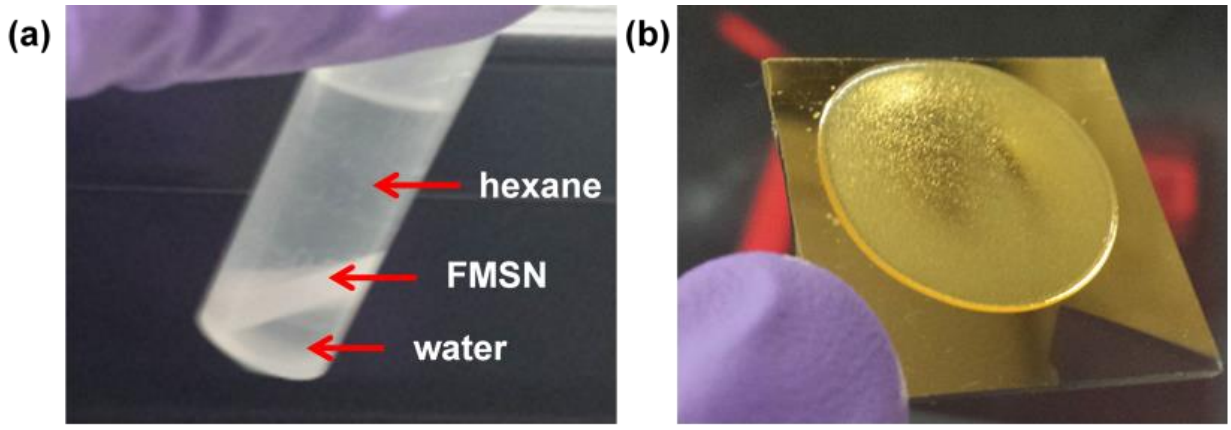

Figure 2.40. The figure on the left (a) shows the layer separation between $LiClO_4$ water, FMSN, and hexane. The second figure (b) shows the polymer membrane coated on the Au/Ti glass slides as the electrode.

Electrochemical measurements were performed on cross section slices of the silica aerogel/polymer composite electrolyte using an electrochemical workstation CHI-790E. The solid electrolyte is pressed between two glass slides with sputtered Ti/Au (50 nm/50 nm) thin film to form a symmetrical cell. Then electrochemical impedance spectroscopy (EIS) is performed at 50 mV in the frequency range of 1MHz to 1Hz. The resulting impedance data is transformed into a Nyquist plot for equivalent circuit fitting by Randle's circuit, to evaluate the bulk resistance (R_{bulk}) of the composite electrolyte and fitted R_{bulk} is used to calculate ionic conductivity according to Eq (5). The surface area is measured with a digital camera and evaluated with the ImageJ program, while the thickness is measured by a digital caliper with a resolution down to 10 μm.

2.3 Results and Discussions

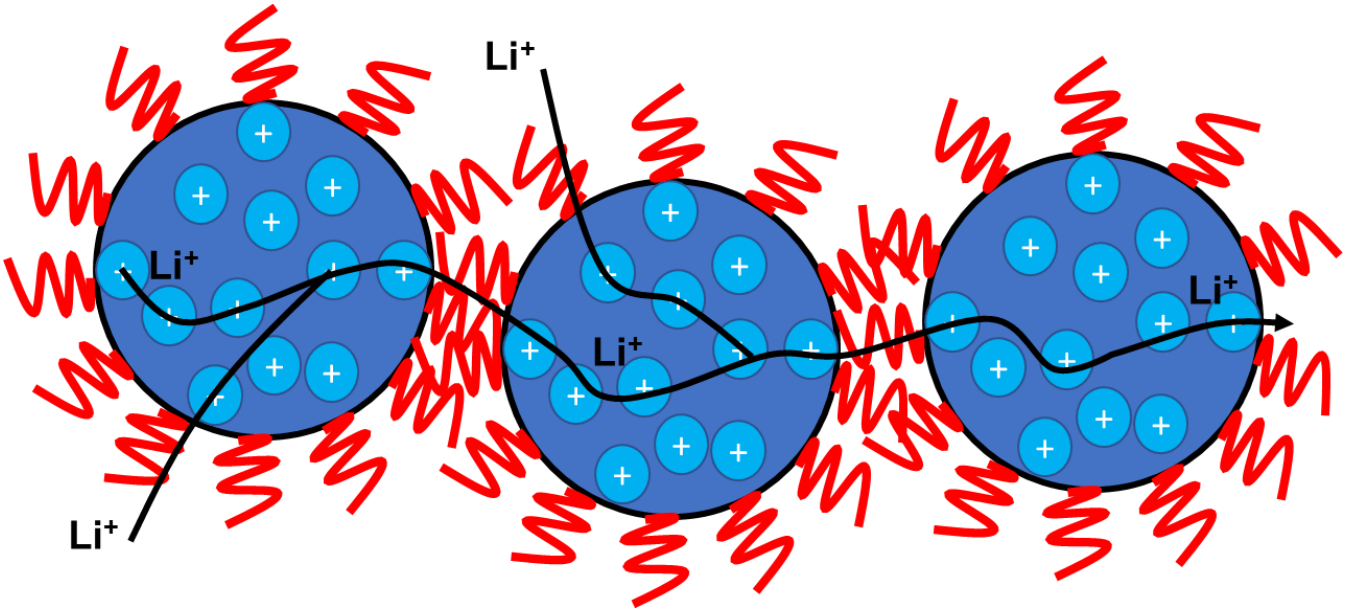

Figure 2.41. The figure shows the Li^+ conduction mechanism in the FMSN once the percolation threshold is reached by addition of FMSN to create a bridge between the two electrodes.

Figure 2.4 schematically illustrates the proposed mechanism for Li^+ conduction through the $LiClO_4$ electrolyte filled pores within the FMSN, thus creating a pathway with high ion conduction from one mesoporous particle to the next. Note the creation of a water pathway for Li^+ to conduct can also offer high ionic conductivity due to the lithium-ion source in the polymer matrix as well, hence the Li^+ joining in the FMSN in the figure. This approach assumes the surface nonpolar hydrocarbon chain does not impede the lithium-ion transfer process, and the hygroscopic nature of the surrounding polymer matrix. In the instance of using PEO, known to be a hygroscopic polymer, can absorb moisture from air, so the wet inner core of the FMSN can be dried and the ionic conductivity will subsequently decrease.

To measure the ionic conductivity of the composite polymer electrolyte, the baseline for the polymer electrolyte must be established to be able to reproduce the ionic conductivity of the measured electrolyte reliably,

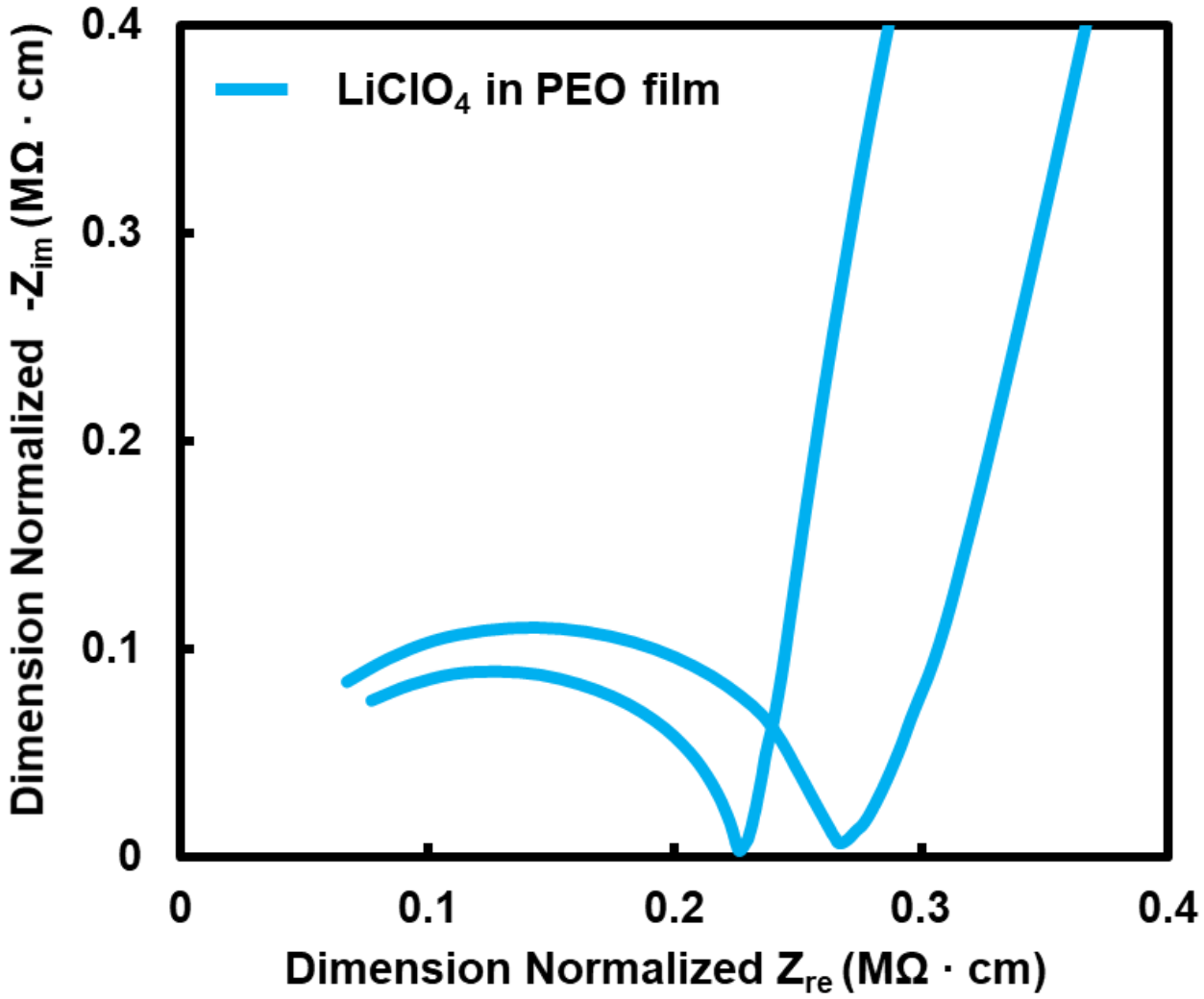

Figure 2.42. The figure shows the Nyquist plot against two different $LiClO_4$ dissolved in PEO samples with the same testing condition to show reproducibility of the symmetrical cell setup with Au/Ti electrodes.

In the figure 2.5, two different samples of the PEO electrolyte membrane were tested for ionic conductivity of the material. The results were 4.2 x 10^{-6} S/cm and 3.8 x 10^{-6} S/cm to represent close reproducibility for future ionic conductivity measurement. Note the typical improvement to the ionic conductivity of solid electrolytes are only noteworthy if the increase it by several factors or orders of magnitude. This is primarily due to the comparison of solid electrolyte to their liquid counterpart, which sets the requirement to 10^{-3} S/cm.

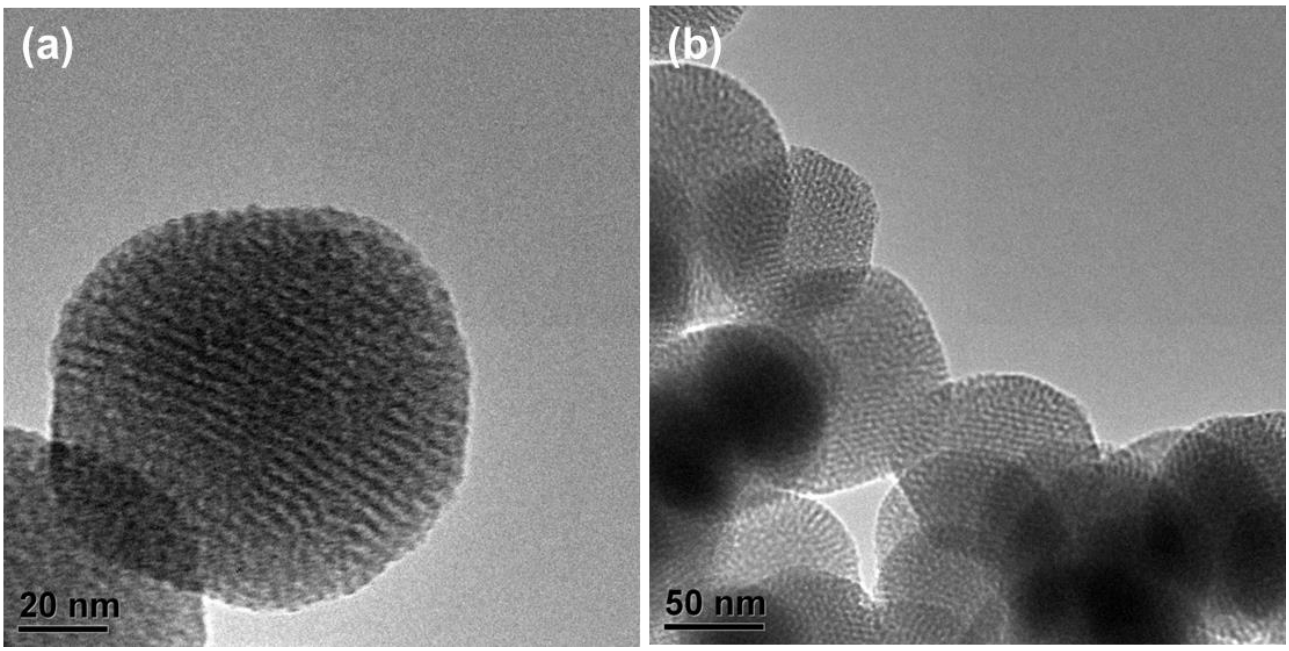

Figure 2.43. The figure shows the as made MSN in (a) zoomed in on a single particle with scale bar at 20 nm, and (b) cluster of mesoporous silica nanoparticle with scale bar at 50 nm, and the estimated pore size being 2 to 3 nm in diameter. The average nanoparticle size are ~ 100 nm.

Transmission electron microscopy is done on the mesoporous silica nanoparticles to show the pore size to be 2 to 3 nm in diameter to show the pores within the porous particle are connected to one another (Figure 2.6 a,b). Therefore, this would allow ample volume for Li^+ to

pass through within the pores when the voltage is applied. The imaging of the mesoporous silica nanoparticle confirms the average size of the nanoparticles to be about spherical in shape with average diameter of 100 nm. Interestingly, regardless of the size of the mesoporous silica nanoparticle, the percolation threshold for spherical object in a volume is 20% of the volume. However, for performance purpose, as many connections between the electrodes as possible. This is due to the bulk ionic conduction nature of the electrolyte needing as many possible pathways as the material allows. But for the purpose to demonstrate viability of the composite solid polymer electrolyte, 300 mg of functionalized mesoporous nanoparticles to 400 mg of PEO is used instead.

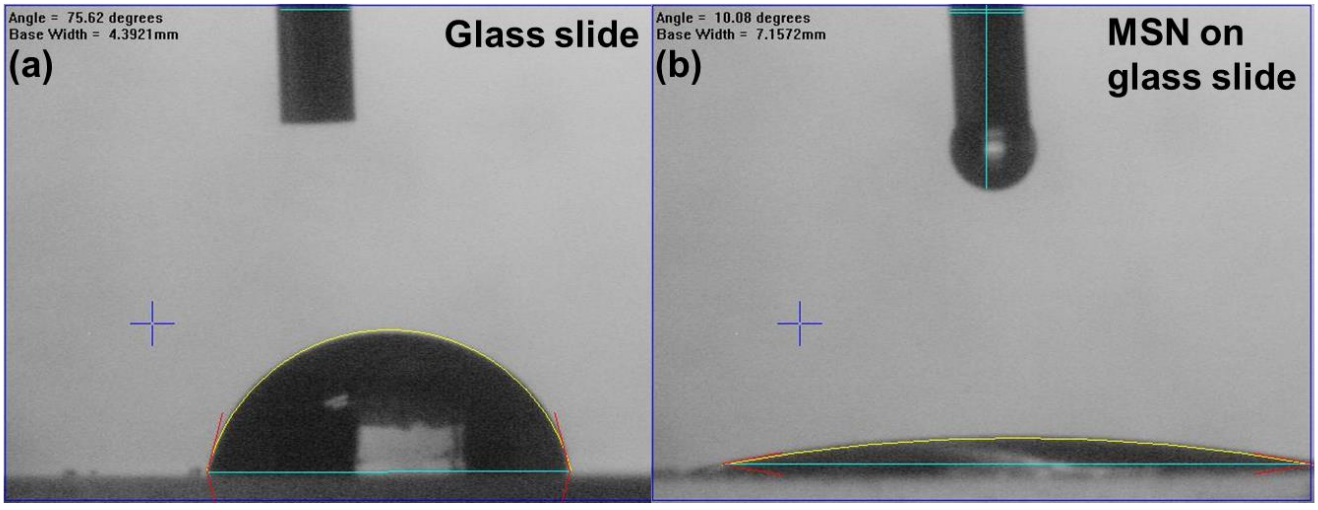

Figure 2.44. The figure demonstrates the contact angle measurement on (a) glass slide with the water droplet contact angle of 75.62 º and base width of 4.39 mm and (b) MSN coated glass slide with the water droplet contact angle of 10.08 º and base width of 7.16 mm.

To further understand the wettability of the silica surface to attract water, a contact angle measurement is conducted using a dropper filled with distilled water. The setup consists of a light source projecting light across the platform with the sample stage, the light is then projected

into a mirror and reflected into the detector. The image can then be processed by computer program to measure contact angles. The functionalized mesoporous silica nanoparticles and mesoporous silica nanoparticles are coated on the glass slides by spray coating with an air spray connected to an oxygen tank. The droplet on top of the glass slide as the standard shows a water droplet contract angle of 75.62^{o} (Figure 2.7 a), which suggests the glass slide as hydrophilic in nature, and that is consistent with the expectation. When the water droplet is placed on as made mesoporous silica nanoparticles, and the distilled water droplet is flattened quickly, with contact angle of 10.08^{o} (Figure 2.7 b). This suggests that the mesoporous silica nanoparticle is more hydrophilic than the glass slide surface, which makes an excellent material for storage of aqueous $LiClO_4$ electrolyte as the capillary action holds the electrolyte in and allow for formation of linked electrolyte filled nanoparticles.

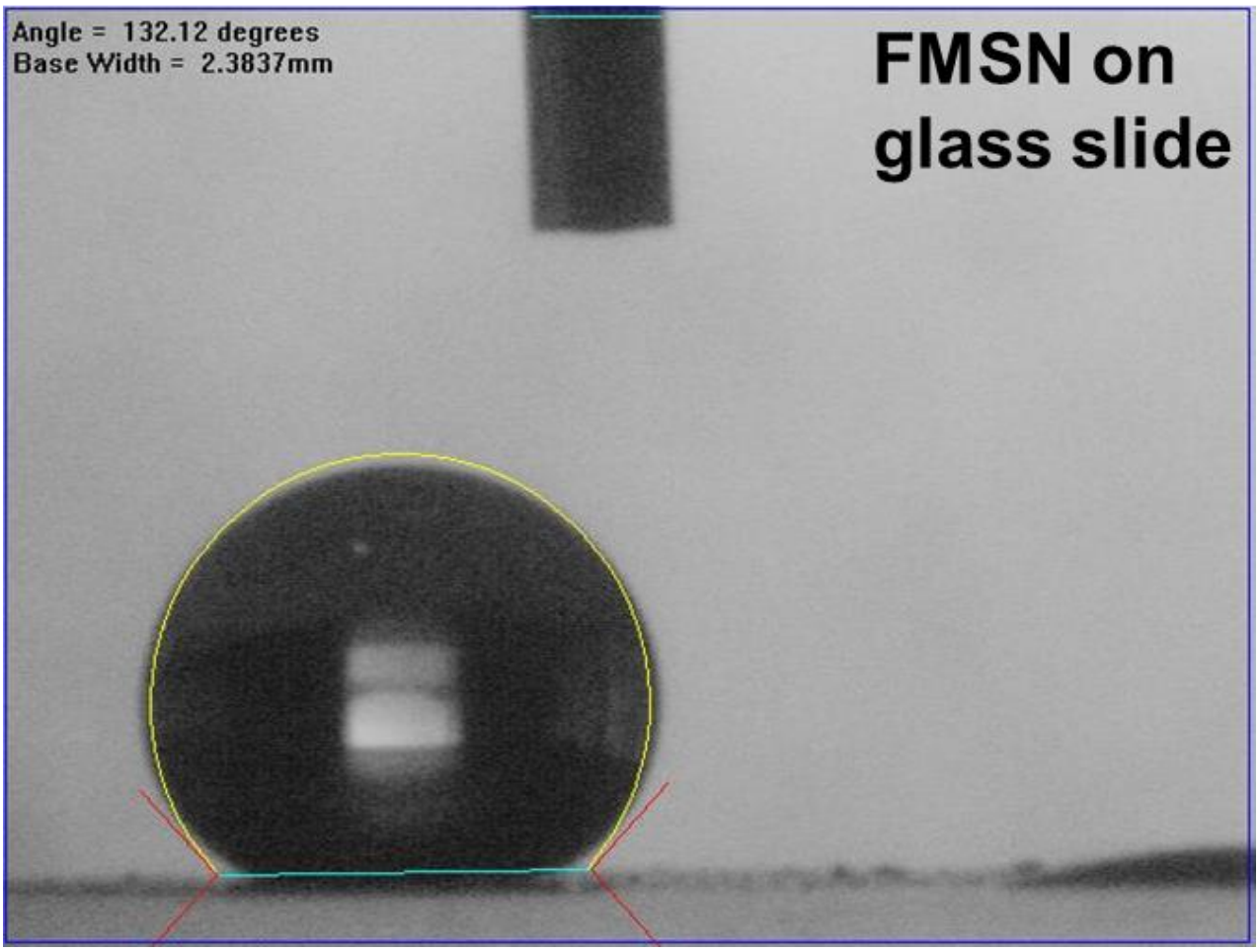

Figure 2.45. The figure shows the water droplet contact angle measurement on a glass slide coated with functionalized mesoporous silica nanoparticles. The contact angle of the water shows 132.12 º and 2.38 mm of base width.

The contact angle measurement of the water droplet on the FMSN coated glass slide is 132.12º, which means the functionalized mesoporous silica nanoparticles are hydrophobic and repels water (Figure 2.8). This makes an excellent outer functional group for the mesoporous structure to contain water, as the water is trapped within the nanoparticle with a sphere of nonpolar groups that forces the $LiClO_4$ in the nanoparticle.

The mechanism that causes hydrophilicity and hydrophobicity is entirely dependent on interfacial energy and surface tension. As the droplet is placed on the surface of a material, there are three separate interactions happening, the interaction between the droplet and the air, the droplet and the surface, and the water molecules with each other. In the case of hydrophilic surface area, the water droplet interaction with the surface is more favorable than the interaction between the water droplet and the air. Thus, this forces the water droplet to maximize interfacial area with the surface and minimize the interfacial contact area between water droplet and air. This leads to the water flattening out to obtain the higher ratio between surface area interaction of droplet to surface over droplet to air. Then considering the hydrophobic case, as the droplet is placed on the surface of a material, the interaction of droplet with surface is less favorable compared to the interaction of droplet with air. Thus, the water droplet is forced to maximize the interfacial area with air and minimize the interfacial contact area with the surface below. This leads to the water becoming more spherical to maximize the area of interaction with air. In extreme cases of super hydrophilicity, water droplet coats itself as a thin layer on the surface of the material, and super hydrophobicity is when the water droplet beads up on the surface.

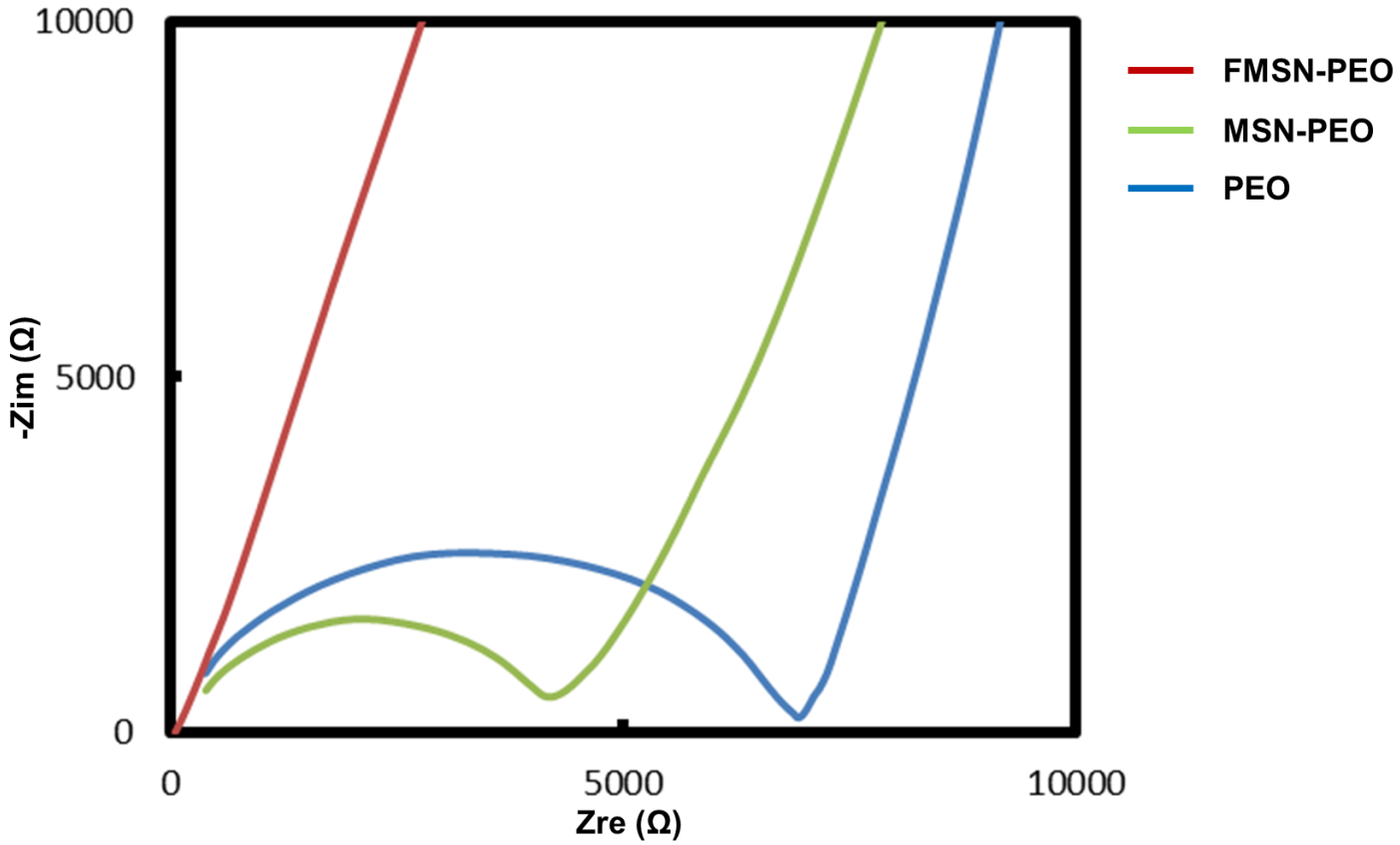

Figure 2.46. The figure shows Nyquist plot of FMSN-PEO composite solid polymer electrolyte (red), MSN-PEO composite solid polymer electrolyte (green), and PEO solid polymer electrolyte (blue). The solid electrolytes were tested in the cell configuration of Au/electrolyte/Au after 5 hours of air drying.

To further study the effects of the water encased nanoparticles during ion transport in the composite electrolyte, we utilize EIS for measurement of ionic conductivity. The samples were dried for 5 hours, in Figure 2.9, before being sandwiched into a symmetrical cell with blocking electrodes for testing. The resulting Nyquist plot shows the presence of semicircle for both MSN-PEO composite solid polymer electrolyte and PEO solid polymer electrolyte. Which can be simulated by a simplified Randles circuit to measure the resistance, from using the equivalent

circuit below (Figure 2.10).

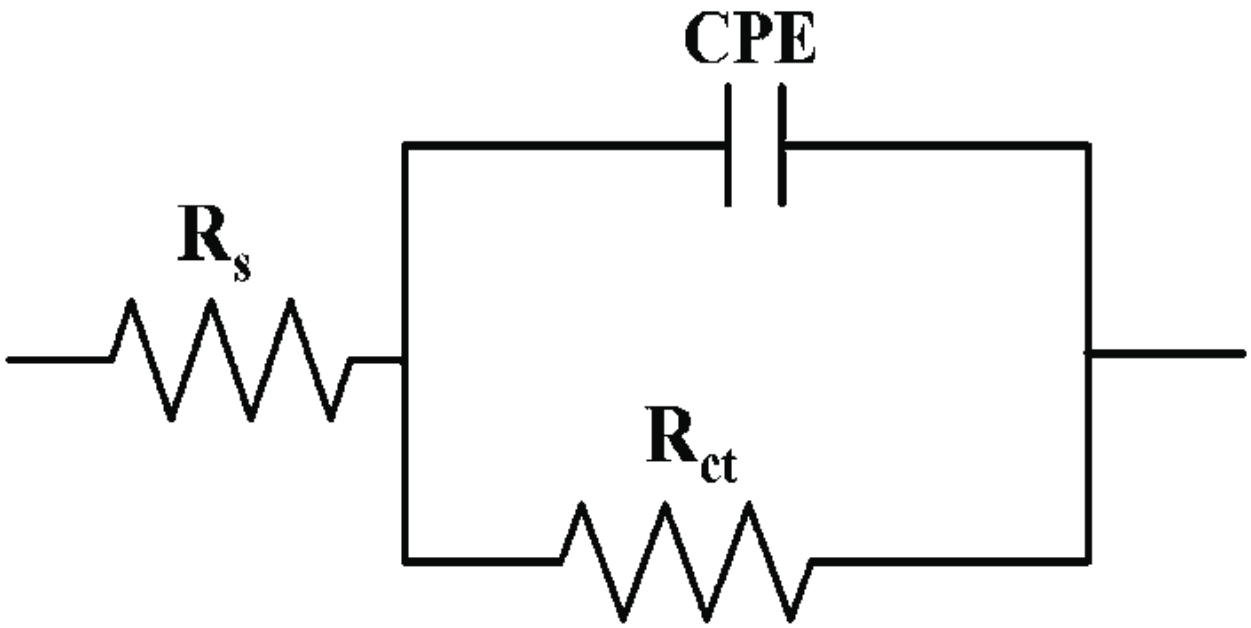

Figure 2.47. The figure shows a simplified Randles circuit for the equivalent circuit fitting of a semicircle, note the lack of Warburg impedance element means the low frequency tail of the Nyquist curve is not accounted for.

The equivalent circuit fitting suggests the MSN-PEO composite solid polymer electrolyte to have an ion transport resistance 4400 Ω, which equates to 2.0 x 10^{-6} S/cm. And the result for PEO solid polymer electrolyte shows ion transport resistance of 7000 Ω, which equates to 1.0 x 10^{-6} S/cm. Interestingly, the FMSN-PEO composite solid polymer electrolyte do not appear to have a semicircle and the low frequency tail does not appear to behave like a capacitor. This means that the ion conduction is still happening, however, at a higher frequency, which could suggest a shift in the ion transport mechanism towards facile transport in the liquid electrolyte channel rather than the slower transport through the PEO polymer.

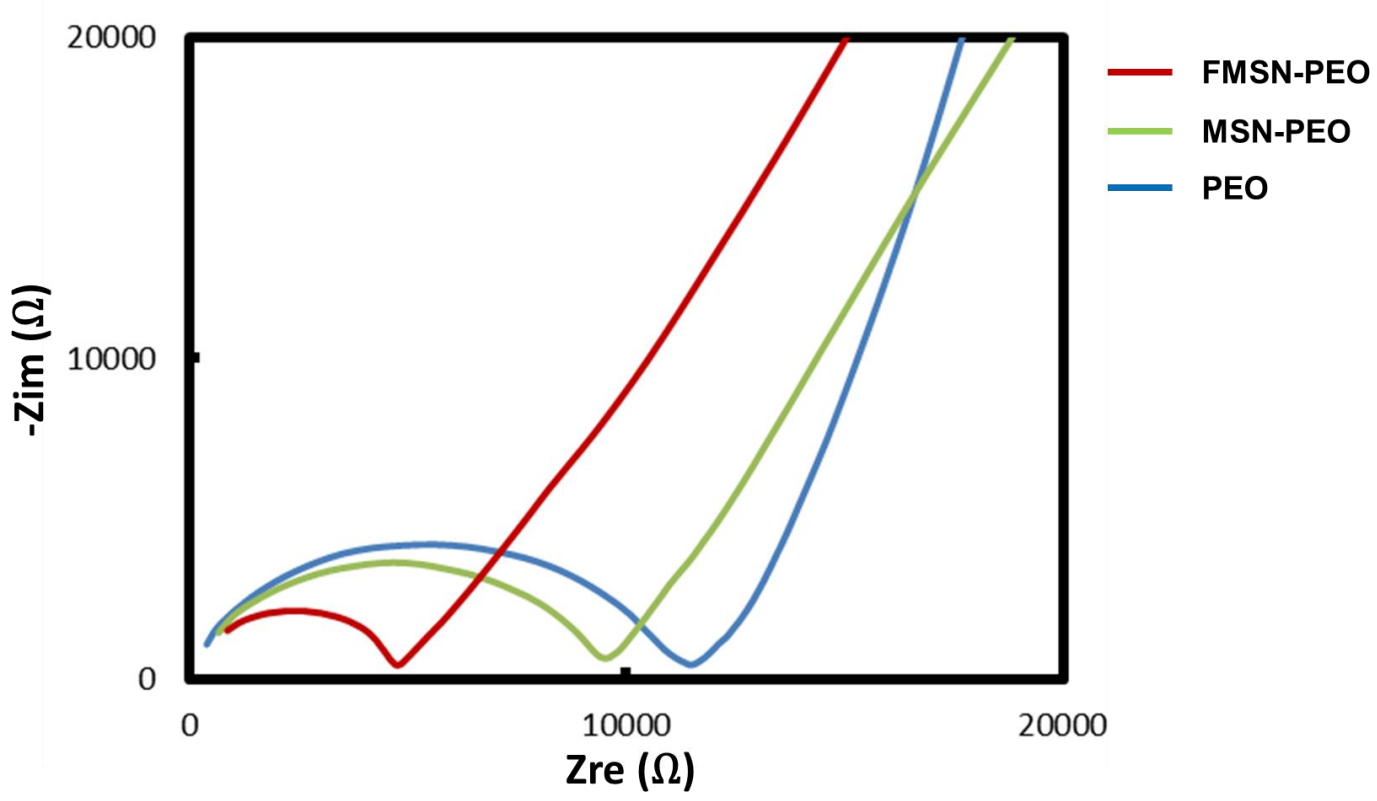

Figure 2.48. The figure shows Nyquist plot of FMSN-PEO composite solid polymer electrolyte (red), MSN-PEO composite solid polymer electrolyte (green), and PEO solid polymer electrolyte (blue). The solid electrolytes were tested in the cell configuration of Au/electrolyte/Au after 9 hours of air drying.

However, further drying process of the solid polymer electrolyte reveals the ionic conductivity of the solid polymer electrolytes to be largely dependent on the acetonitrile in the polymer, which further reduces the already low ionic conductivity of the FMSN-PEO composite solid polymer electrolyte. From simplified Randles circuit fitting of the Nyquist curves (Figure 2.11), it is revealed that the ionic conductivity of PEO solid polymer electrolyte is lowered to 7.0×10^{-7} S/cm, the MSN-PEO composite solid polymer electrolyte's ionic conductivity is lowered to 9.0×10^{-7} S/cm. And the semicircle begins to appear for FMSN-PEO composite solid polymer

electrolyte, which 1.5 x 10^{-6} S/cm when the dimension of the membrane is factored in. This presents itself as a performance shortfall when compared to the lower limit requirement for solid polymer electrolyte to achieve ionic conductivity of 10^{-3}.

2.4 Conclusion

In conclusion, to address the charge and discharge rate challenge for the existing lithium-ion battery requires innovative approaches. Limitations that organic liquids can be explored in other electrolyte system, such as the composite solid polymer electrolytes. Targeted approach to address the needs of high ionic conductivity for these composite solid polymer electrolytes to achieve ionic conductivity of 10^{-3} S/cm has yet to be fully explored. In our effort, we were able to recognize methods to create facile ion transport to assist the composite solid polymer electrolytes to achieve the required ionic conductivity. In addition, we established standard method for measuring ionic conductivity by utilizing EIS and Nyquist plot fitting with equivalent circuit. We further demonstrated the trapping of $LiClO_4$ liquid electrolyte in the mesoporous silica nanoparticle by using a core-shell structure composed of a hydrophilic core for liquid electrolyte storage and a shell of hydrophobic functional group that acts as encasement for the liquid inside. Though we showed ionic conductivity of FMSN-PEO composite solid polymer electrolyte to be promising after short period of air drying, the 9-hour air drying sample indicates the composite solid polymer to be unable to compete against the required 10^{-3} S/cm. Furthermore, the rapid decrease in ionic conductivity indicates a that the ion conduction mechanism is still largely depending on the polymer matrix of composite solid electrolyte. This also indicates the required improvement to both phases in the composite material for ionic

conductivity of composite solid polymer electrolyte to be incorporated in actual lithium-ion batteries.

2.5 Reference

1. Jung, D. Y., Lee, B. H. & Kim, S. W. Development of battery management system for nickel-metal hydride batteries in electric vehicle applications. *J. Power Sources* **109**, 1–10 (2002).

2. Köhler, U., Kümpers, J. & Ullrich, M. High performance nickel-metal hydride and lithium-ion batteries. *J. Power Sources* **105**, 139–144 (2002).

3. Müller, T. & Friedrich, B. Development of a recycling process for nickel-metal hydride batteries. *J. Power Sources* **158**, 1498–1509 (2006).

4. Reddy, M. V., Mauger, A., Julien, C. M., Paolella, A. & Zaghib, K. Brief history of early lithium-battery development. *Materials (Basel).* **13**, 1–9 (2020).

5. Presentations & Videos - QuantumScape. Available at: https://www.quantumscape.com/technology/presentations-videos/. (Accessed: 23rd June 2021)

6. QuantumScape building electric car battery that charges to 80% in 15 minutes. Available at: https://www.cnbc.com/2020/12/08/quantumscape-building-electric-car-battery-that-charges-to-80percent-in-15-minutes.html. (Accessed: 23rd June 2021)

7. Masaki Yoshio, H. N. *Lithium-Ion Batteries, Chapter 2*. *Lithium-Ion Batteries* (2009).

8. Plichta, E. J. & Behl, W. K. Low-temperature electrolyte for lithium and lithium-ion

batteries. *J. Power Sources* **88**, 192–196 (2000).

9. Dahbi, M., Ghamouss, F., Tran-Van, F., Lemordant, D. & Anouti, M. Comparative study of EC/DMC LiTFSI and LiPF6 electrolytes for electrochemical storage. *J. Power Sources* **196**, 9743–9750 (2011).

10. Zhang, S. S. Liquid electrolyte lithium/sulfur battery: Fundamental chemistry, problems, and solutions. *J. Power Sources* **231**, 153–162 (2013).

11. Abouimrane, A., Ding, J. & Davidson, I. J. Liquid electrolyte based on lithium bis-fluorosulfonyl imide salt: Aluminum corrosion studies and lithium ion battery investigations. *J. Power Sources* **189**, 693–696 (2009).

12. Quartarone, E. & Mustarelli, P. Review—Emerging Trends in the Design of Electrolytes for Lithium and Post-Lithium Batteries. *J. Electrochem. Soc.* **167**, 050508 (2020).

13. Rao, M., Geng, X., Liao, Y., Hu, S. & Li, W. Preparation and performance of gel polymer electrolyte based on electrospun polymer membrane and ionic liquid for lithium ion battery. *J. Memb. Sci.* **399**–**400**, 37–42 (2012).

14. Xu, D. *et al.* In Situ Generated Fireproof Gel Polymer Electrolyte with Li6.4Ga0.2La3Zr2O12 As Initiator and Ion-Conductive Filler. *Adv. Energy Mater.* **9**, (2019).

15. Li, G., Li, Z., Zhang, P., Zhang, H. & Wu, Y. Research on a gel polymer electrolyte for Li-ion batteries. *Pure Appl. Chem.* **80**, 2553–2563 (2008).

16. Stephan, A. M. Review on gel polymer electrolytes for lithium batteries. *Eur. Polym. J.* **42**, 21–42 (2006).

17. Egashira, M., Todo, H., Yoshimoto, N. & Morita, M. Lithium ion conduction in ionic liquid-based gel polymer electrolyte. *J. Power Sources* **178**, 729–735 (2008).

18. Liu, M. *et al.* Novel gel polymer electrolyte for high-performance lithium-sulfur batteries. *Nano Energy* **22**, 278–289 (2016).

Chapter 3. Application and Synthesis of Nanomaterials and Solid-State Materials in High Energy Density Batteries

3.1 Introduction

Lithium metal battery, not to be confused with conventional lithium-ion battery, have garnered a lot of interest in the mobile phone and electric vehicle market as an improvement upon existing battery technology.[1–5] This is due to the specific capacity between the lithium metal anode (3840 mA h/g) compared to the existing conductive carbon anode (372 mA h/g). By replacing materials with lithium metal that stores more charge, the overall energy density of the whole battery can be increased, which applies to the cathode material as well. However, to achieve this, the fundamental problem of lithium dendrite growth during charge and discharge will have to be addressed.[6–8] One promising material to address this problem is the solid-state electrolyte, though lacking in ionic conductivity (10^{-3} S/cm to 10^{-5} S/cm), the composite solid electrolyte has been extensively explored to have both high ionic conductivities, approaching 10^{-3} S/cm, and high Young's Moduli.[9,10] Yi Cui group at Stanford has extensively investigated the effects on solid electrolyte performance when different nanomaterial being incorporated in traditional solid polymer electrolyte.[11–13] Notably is the ionic conductivity improvement to common solid polymer electrolyte like polyethylene oxide (PEO) when nanostructure like silica aerogel is infused with PEO and LiTFSI salt. In the publication, improvement of ionic conductivity from 10^{-5} S/cm to 10^{-4} S/cm. Similarly, silica nanoparticles have also been shown to improve ionic conductivity as well.[14,15] However, the mechanism for this improvement is not well understood. Publications have contributed the effects to interfacial transport, crystallinity disruption, and surface group interactions for the increase in ionic conductivity.[16,17]

The composite solid polymer electrolyte is composed of two separate components, the polymer matrix and the inorganic solid, and usually with a salt source to provide the ions for the active electrodes. Some common polymer matrix (Figure 3.1) that has good ionic conductivity are polyethylene oxide (PEO) with 10^{-5} S/cm, polyvinyl pyrrolidone (PVP) with $2x10^{-5}$ S/cm, polyvinyl sulfide (PVS) $4x10^{-4}$ S/cm, and polyvinyl (PVDF) with $7x10^{-4}$ S/cm.[18–22]

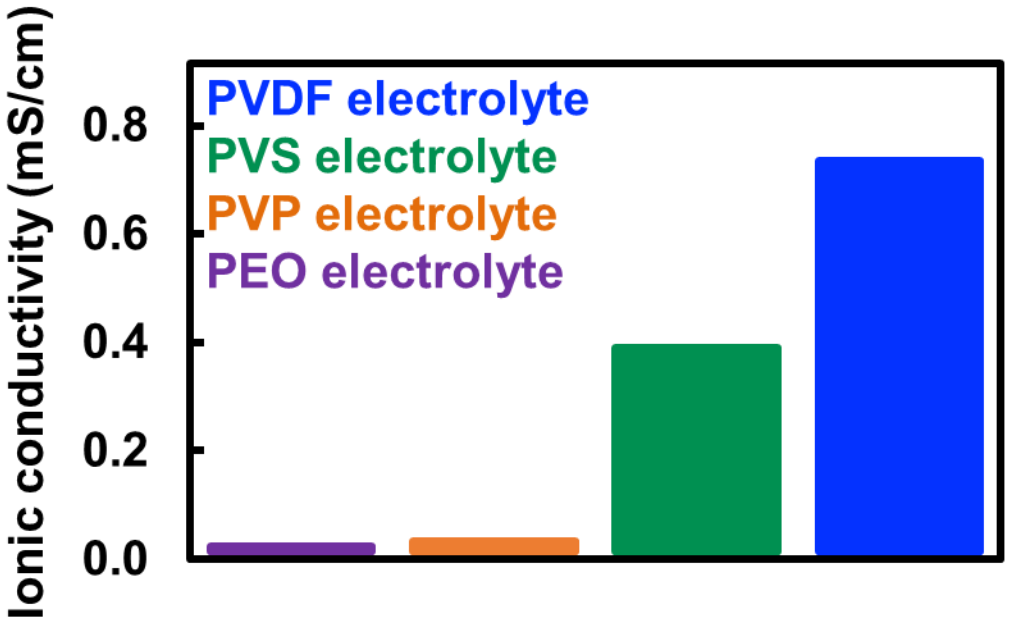

Figure 3.49. Figure shows the ionic conductivity of PEO, PVP, PVS, and PVDF electrolyte with lithium salt compared to each other. The purple bar represents PEO electrolyte, orange bar is the PVP, green bar is the PVS, and blue bar is the PVDF.

Note the common solid polymer electrolytes have polymer chains with electronegative groups which stabilizes the lithium ion during ion conduction process. These functional groups can aid in the ion process through either dipole-dipole interactions or electrostatic interactions when the functional group is charged. The second component is composed of inorganic solids, they can be either ionically conductive or inert. In the instance of ionically active solids,

examples like LLTO and LLZO have been extensively studied[23,24] in a variety of nanostructures, such as nanoparticles and nanowires. They typically show high ionic conductivity of 10^{-4} S/cm alone, the addition of polymer matrix is for the structural stability. While the inert nanostructures like silica nanoparticles and silica aerogels contributes mainly rigid structural support to the polymer matrix, recent publications have also shown the increase to ionic conductivity for the electrolyte when inert solids are introduced.

Here we propose improvement to ionic conductivity of composite solid-state electrolyte by introducing modified and unmodified high surface area material with three-dimensional structure to ensure the creation of percolating pathway for lithium ion to conduct. We demonstrate the ion conduction improvement of composite solid polymer electrolyte by using high surface area nanostructure as the inert inorganic material and LiTFSI dissolved in PEO as the polymer matrix, where the Li^+ conducts primarily through the polymer. We show that both silica aerogel and hexagonal boron nitride aerogel (hBN) improves the ionic conductivity of the polymer matrix. The silica aerogel infused with PEO shows ionic conductivity of $2x10^{-5}$ S/cm and the hBN aerogel infused with PEO shows ionic conductivity of $5x10^{-5}$ S/cm. This is an order of magnitude improvement compared to the standard PEO polymer electrolyte with ionic conductivity between $3.6x10^{-6}$ S/cm to $4.4x10^{-6}$ S/cm. We also demonstrated the thin film of stacked MoS_2 nanosheets and PVP binder to also exhibit ionic conductivity after intercalation with lithium ions.

3.2 Experimental

Silica aerogel is made by basic solution containing tetraethyl orthosilicate (TEOS) to make the sol gel. Briefly, the base solution is made with 23.0 mL of ammonium hydroxide solution, ACS grade, 28.0 – 30.0% NH_3 basis is mixed in 100 mL of water, then 2.0 g of ammonium fluoride is dissolved in the mixture. Next, a fresh 40 mL of water and 60 mL of ethanol is prepared, followed with the addition of 2.0 mL of ammonium hydroxide/ ammonium fluoride solution prepared to make the basic solution. The precursor solution is made with mixing 25.0 mL of TEOS, reagent grade 98%, and 50.0 mL of ethanol. When preparing the sol gel, a ratio of 1:1 precursor solution and basic solution for 3 minutes before casted into a mold of desired shape, the mold is made of polyethylene or Teflon. After 30 minutes, gelation of the solution makes a free-standing silica sol gel that is placed in ethanol solution to be solvent exchanged overnight before solvent exchanged with acetone for a day. The free-standing silica sol gel is then placed in a supercritical dryer with liquid CO_2 to exchange out the acetone before passing the supercritical point and dried to form the free-standing silica aerogel.

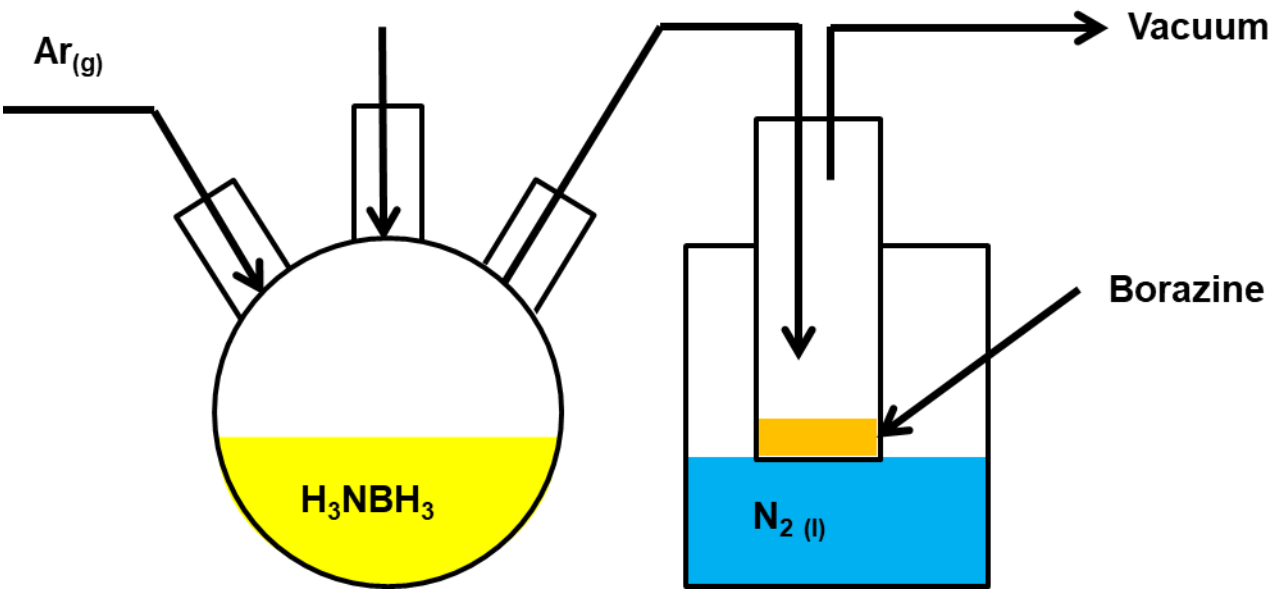

Figure 3.50. The figure shows the setup for collecting borazine (orange) from decomposition of ammonia borane, H_3NBH_3 (yellow). The ammonia borane is in tetraethylene glycol dimethyl ether in the three neck round bottom flask with argon flow, and a cold trap with vacuum applied.

The hBN aerogel is prepared by template assisted chemical vapor deposition (CVD) method.[25,26] Briefly, the borazine precursor was prepared with thermal decomposition method. 40 g of ammonia borane is dissolved in 100 mL of tetraethylene glycol dimethyl ether and heated to 110 ^{o}C under 50 mbar, borazine vapor is collected in a liquid nitrogen collection trap as a clear and colorless liquid (Figure 3.2). The template for the hBN aerogel is the graphene aerogel, starting with graphene oxide (GO) prepared according to modified Hummers' method.[23,24] A GO 10 mL solution with 5.0 mg/ mL concentration was mixed with 60 µL of ethylenediamine and 50 µL of sodium borate solution, 5 % wt, and well mixed before being separated into homemade reaction vessels and placed in a Teflon autoclave in an oven under 120^{o}C overnight to form the graphene sol gel. The graphene sol gel is then solvent exchanged in an ethanol solution overnight

before being frozen and placed in a freeze dryer overnight to make the graphene aerogel (GA). The GA is then placed in a vacuum applied quartz tube with a home-made bubbler is used to introduce the borazine precursor at an Ar flow rate of 10 sccm and the chamber is sealed when the chamber pressure reaches 150 mbar. The reaction chamber is then heated 500 ^{o}C and held to 1 hour in a high temperature annealing furnace to generate the polyborazylene and deposited on the GA. Then the reaction chamber is heated to 1500 ^{o}C for 3 hours to generate amorphous BN on the surface of GA via dehydrogenation reaction before hBN is formed. Next, the CVD deposited hBN assisted by GA is annealed again at 600 ^{o}C in air to etch away the GA template, and the free-standing hBN aerogel is made.

The hBN and silica aerogel composite solid polymer electrolyte are made by vacuum infusion method with monomer solution of the PEO and LiTFSI. Briefly, 5.6 g of polyethylene glycol diacrylate (PEGDA) with average Mn ~700 mixed with 3.7 g of butanedinitrile, 4.2 g of Bis(trifluoromethylsulfonyl)amine lithium salt (LiTFSI) and 56 mg of phenylbis(2,4,6-trimethyl-benzoyl) phosphine oxide photoinitiator to form the monomer solution. The hBN or silica aerogels are then submerged in the monomer solution in a glass container and placed in a vacuum chamber to infuse the aerogel with the monomer solution for 1 hour. The resulting material was a free-standing monomer electrolyte and aerogel composite or hBN composite. The composite is then placed under a 254 nm ultraviolet lamp for 20 minutes for crosslinking of PEGDA to form PEO, resulting in a free-standing aerogel/polymer composite electrolyte. All steps for monomer solution preparation prior to photocuring are enclosed in a dark vial to prevent external light source from photopolymerizing the monomer prior to photocuring process.

Electrochemical measurements were performed on cross section slices of the silica aerogel/polymer or hBN/polymer composite electrolyte using electrochemical workstation

CHI790E. The solid electrolyte is pressed between two glass slides with sputtered Ti/Au (50 nm/50 nm) thin film to form a symmetrical cell. Then ac impedance spectroscopy (EIS) is performed at 50 mV in the frequency range of 1MHz to 1Hz. The resulting impedance data is transformed into Nyquist plot for equivalent circuit fitting by Randle's circuit, to evaluate the bulk resistance (R_{bulk}) of the composite electrolyte. The fitted R_{bulk} is used to calculate ionic conductivity according to Eq (5). The surface area is measured with a digital camera and ImageJ program, while the thickness is measured by a digital caliper with resolution down to 10 μm.

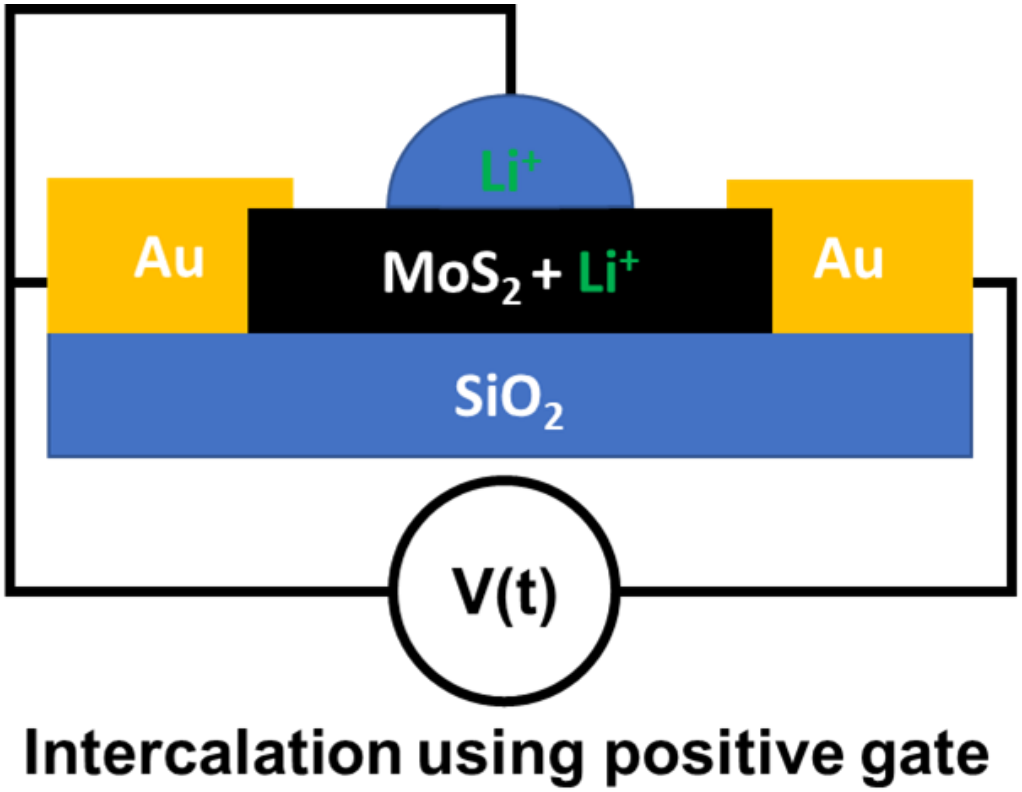

Figure 3.51. The figure shows the Li^+ intercalation process, the MoS_2 film (5 μm thick) is connected on the left and right by the deposited Au and supported by a glass slide. A drop of 1.0 M $LiClO_4$ solution is then placed on top of the MoS_2 film, electrodes are attached to the Au electrodes and the droplet.

The MoS_2 thin film device (Figure 3.3) were made by spin coating of MoS_2 multilayer sheets suspension in dimethylformamide (DMF). Briefly, pristine bulk MoS_2 were attached to duck-mouth copper clip with the MoS_2 being the electrode. The MoS_2 is submerged in a solution of 200 mg $LiClO_4$ salt and 40 mL DMF, the MoS_2 is connected to a power supply and a copper wire is inserted in the solution to complete the circuit. A 3 V potential is applied across the MoS_2 and copper wire, the lithium ion is intercalated into the MoS_2 causing rapid volume expansion of the MoS_2 flake. The expanded flake is then placed in a 40 mL DMF solution containing 0.8 g PVP with Mn of 40000. The solution is then sonicated with the expanded flake for 2 hours resulting in an ink solution. The ink solution is then solvent exchanged with fresh DMF several times with using a centrifuge before a dilute ink solution is formed with MoS_2 flakes as a suspension. The ink is then spin coated onto cleaned glass slides surface with tape covering. A layer of aluminum foil is used to cover the MoS_2 thin film, and then gold is deposited overnight for electrode contact. Afterwards, the aluminum protector is taken off to make the symmetrical cell with configuration of Au/MoS_2 thin film/Au supported by the glass slide.

3.3 Results and Discussions

The 3D nanostructure of the hBN aerogel, silica aerogel, and MoS_2 exhibit unique morphological environment for lithium-ion transport in the composite solid-state electrolyte compared to conventional random placement of nanoparticles in the composite (Figure 3.4 a). First, inert inorganic nanostructure such as hBN and silica aerogel (Figure 3.4 b) offer greater structural support to the soft polymer electrolyte, therefore increases to the Young's Modulus. Second the unique percolating nature of the aerogel in the composite electrolyte creates a 3D network providing direct pathways for ion conduction. Lastly, the aerogel materials provide high

surface area for surface group interaction to stabilize Li^+ in the case of silica aerogel with the addition benefit of a percolating surface.

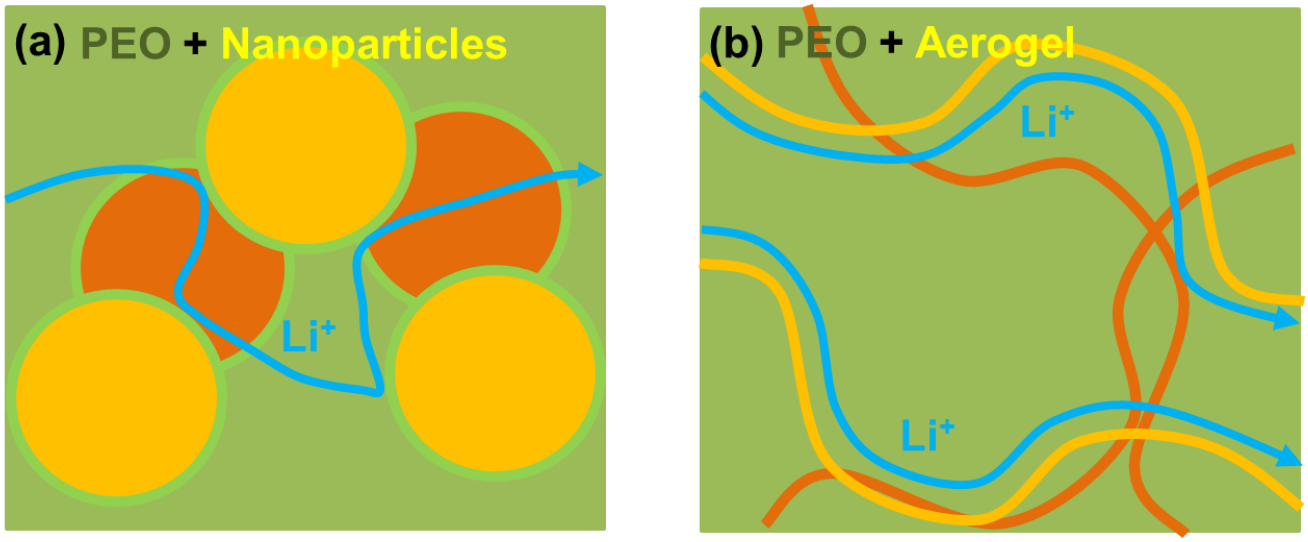

Figure 3.52. The figure shows the blue pathway of lithium ion (Li^+) through the composite solid electrolyte with (a) lithium ion passing through the green PEO matrix with yellow spheres as nanoparticles in the foreground and brown spheres as nanoparticles in the background. (b) The pathway of lithium ion through the green PEO matrix with yellow lines as percolating pathways, and brown lines as aerogel network in the background.

The hBN aerogel and silica aerogel exhibit very different mechanical properties and optical properties. For the hBN aerogel (Figure 3.5 a), the aerogel is nontransparent and reversible against compression. During the infusion process with the PEGDA monomer unit, the structure of the hBN tend to expand rapidly. This is largely due the nanostructure of the hBN aerogel is largely held together by stacking sheets of hBN with van der Waals force between, and due to van der Waals force being a short-range force, the sheets rapidly lose contact with one another. And as a result, without proper PEGDA monomer volume to hBN aerogel ratio, the hBN aerogel falls apart in the PEGDA solution. The silica aerogel on the other hand shows

greater transparency compared to hBN aerogel. However, silica aerogel (Figure 3.5 b) is not capable of reversible compression, this is due to the structural nature of silica. The silica aerogel is composed mainly of connected silica particles with uncontrolled size. The silica aerogel contains mostly air, 99.8% by volume are composed of air.

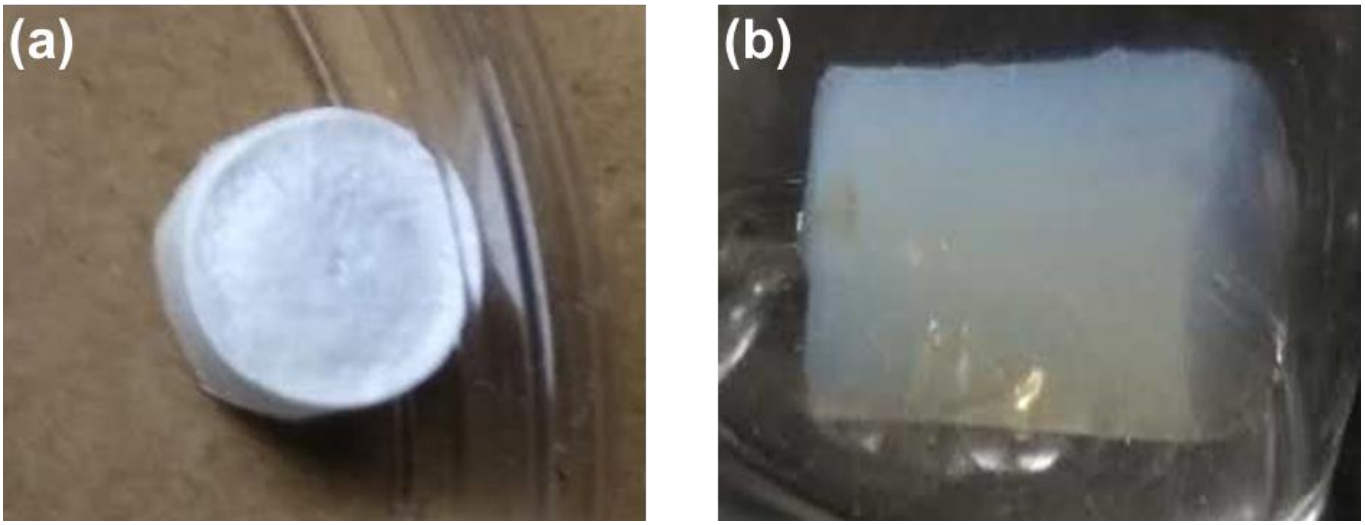

Figure 3.53. The figure shows (a) hBN aerogel in the cylindrical shape, and (b) the silica aerogel in cylindrical shape and partially transparent.

While the mechanical and optical behavior between the two materials is different, the effects of the aerogel as the inorganic component of the composite solid polymer electrolyte is similar, as both improves ionic conductivity of the solid electrolyte. When the silica aerogel infused with PEO/LiTFSI salt was test by EIS (Figure 4), the equivalent circuit fitting suggests the ionic conductivity of the silica aerogel/PEO electrolyte to be 2.0×10^{-5} S/cm compared to the ionic conductivity of PEO to be 8.3×10^{-6} S/cm. Though the ionic conductivity has been increased, it is still far from the desirable 10^{-3} S/cm for practical use of solid electrolyte. Similar study on silica aerogel infused with PEO have been studied,[27,28] and our results is like other publications for both PEO solid electrolyte and the composite.

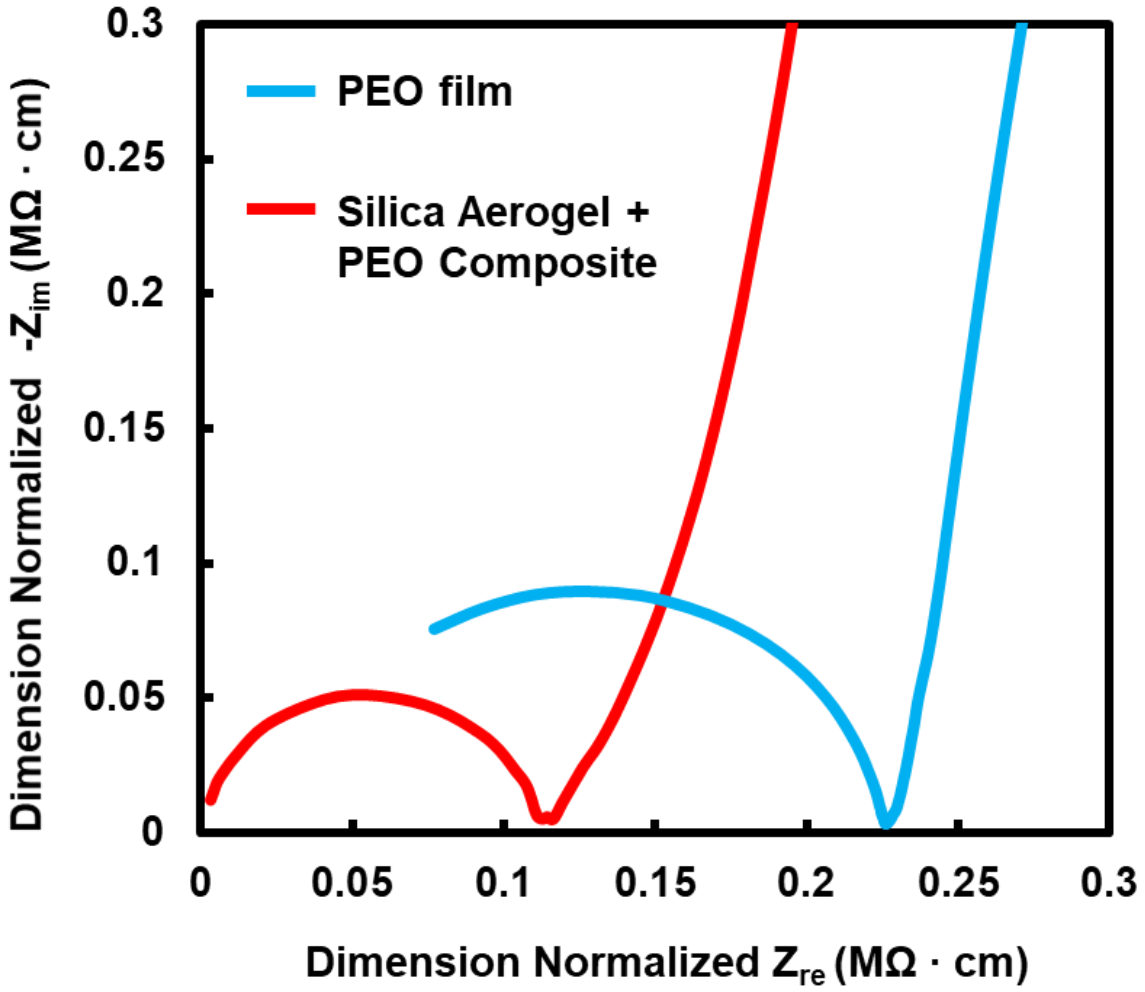

Figure 3.54. The figure shows a 50mV EIS measurement from 1MHz to 1Hz for the solid-state electrolytes (SSE). PEO/LiTFSI solid electrolyte (blue) and silica aerogel infused PEO/LiTFSI composite solid electrolyte (red) sandwiched in the configuration of Au/SSE/Au.

Briefly, the axes are normalized by the dimension of the tested material, this is done to account for differences between samples varying in cross section area and thickness. The semicircle and low frequency tail can be fitted with the Randles circuit (Figure 3.6). The frequency range for the measurements are performed between 1 MHz and 1Hz. Notice the

missing portion of the semicircle, which is due to the semicircle extending beyond the 1MHz high frequency limit. However, the frequency range measurement beyond 1MHz can sometimes lead to inductive noise, where Nyquist curves are not reproducible.

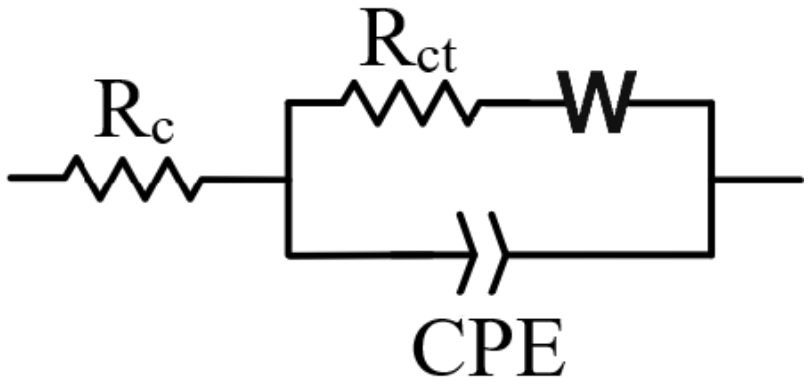

Figure 3.55. The figure shows the Randles circuit, which contains the circuit resistance (R_c) in series to a constant phase element (CPE) in parallel to a series charge transfer resistance (R_{ct}) and Warburg impedance (W).

Thus, electrochemical process within those range cannot be defined, so the Randles circuit fitting (Figure 3.7) assumes there are no additional process happening beyond the 1MHz region. Although the fitting the semicircle to the measured data includes a projected portion, no other electrochemical process is expected at the higher frequency range. Similarly, a modified Randles circuit without the Warburg impedance can also be used to measure the ion conduction resistance or charge transfer resistance (R_{ct}). During the comparison between the two-circuit fitting, no significant difference is seen between them for the R_{ct}.

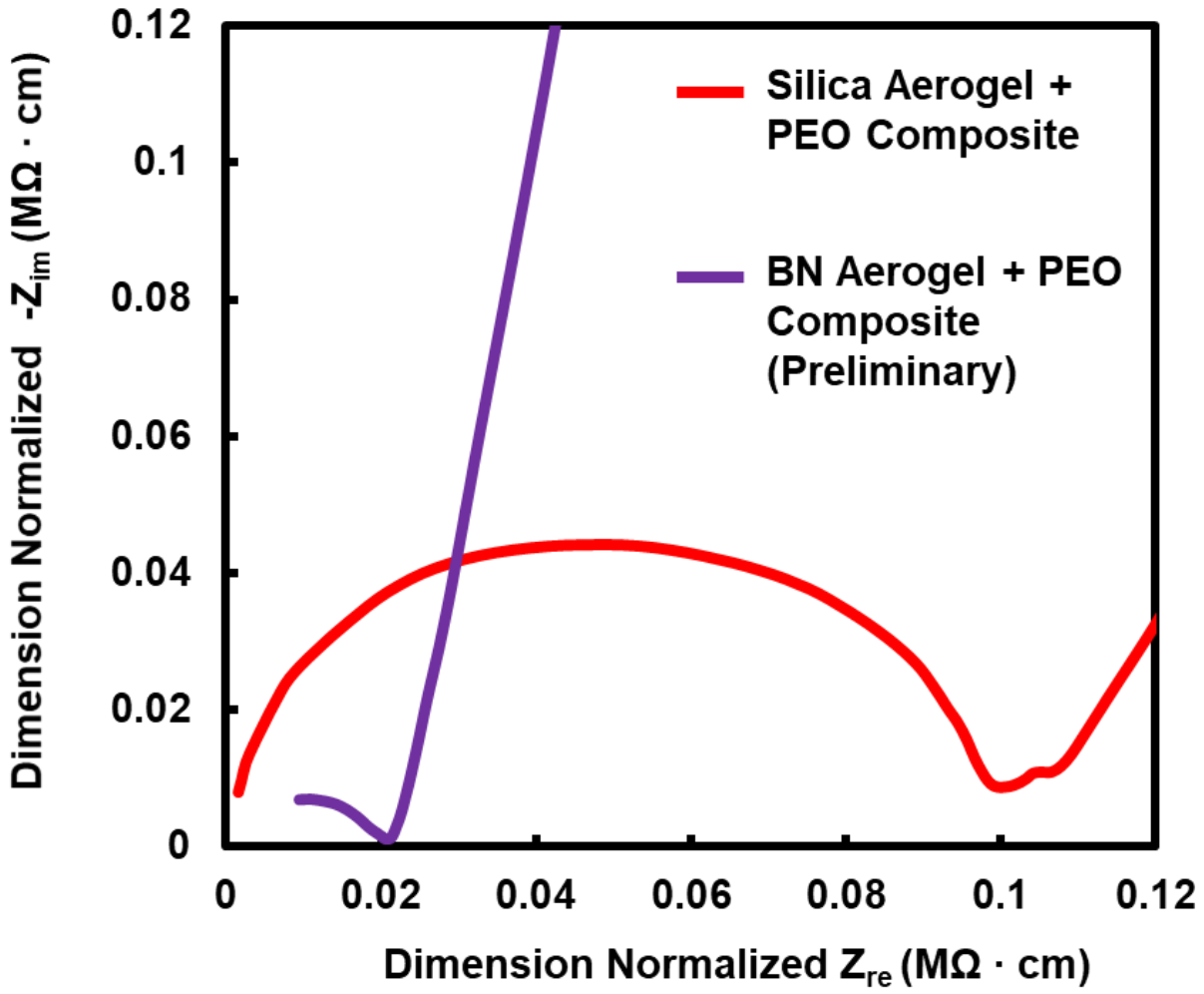

Figure 3.56. The figure shows the direct comparison of the Nyquist curve between silica aerogel infused with PEO/LiTFSI (red) composite and hBN aerogel infused with PEO/LiTFSI (purple) composite.

From the direct comparison of resistivity (Figure 3.8), measured by equivalent circuit fitting using a Randles circuit, between silica aerogel polymer composite electrolyte and hBN aerogel polymer composite electrolyte, in figure 7. We see the ionic conductivity of silica aerogel polymer composite electrolyte is underperforming with ionic conductivity of 2.0×10^{-5} S/cm when compared to the ionic conductivity of 5.0×10^{-5} S/cm for the hBN aerogel polymer

composite electrolyte. We attribute the improvement to ionic conductivity to two coupled factors, firstly, the exceptionally high surface area of the hBN aerogel at 1080 m^2/g,[25,26] and secondly the electronegative nitrogen atom in the honeycomb structured hBN sheets can provide a potential well to stabilize the lithium ion, just as the hydroxyl group on the surface of silica provides a similar interaction to the lithium ion.[13] Thus, the conducting lithium ion in the PEO matrix, typically relying on several electronegative oxygen atoms in the proximity to wrap around the lithium ion to stabilize it, like a hydration sphere for ions.[29–31] The conducting lithium ion would then hop across ideal sites, where the surrounding oxygen atoms create a sufficient potential well to stabilize the lithium ion. In the case of hBN aerogel, due to the 3D structure of the aerogel creating a percolating surface area during lithium-ion conduction, the lithium ion can be shuttled across the large surface area, while being stabilized at the interface between PEO and hBN sheets by the nitrogen atoms and oxygen atoms. One additional benefit of the hBN sheets is the accessibility of the nitrogen atoms compared to the oxygen groups on PEO. While the transport of the lithium ion in PEO requires amorphous polymer to randomly create stable sites, the hBN sheet has nitrogen atoms in an orderly arrangement across the surface thus allowing continuing stable sites for lithium-ion conduction.

To further explore the lithium-ion conduction on the surface and interface of inorganic solid materials, MoS_2 thin film were also chosen to be tested for ion conduction after intercalation. The MoS_2 thin film device are intercalated with lithium ion to allow deposition of lithium ions between the Au electrodes through interface between the MoS_2 sheets in figure 9.

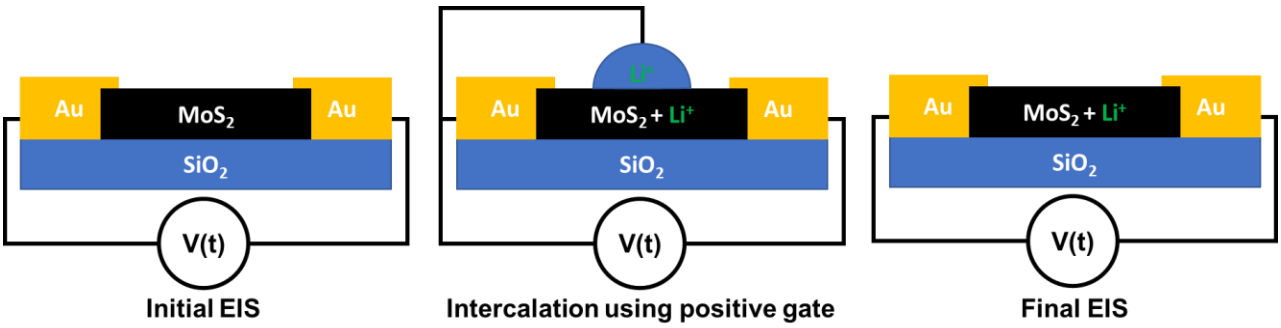

Figure 3.57. The figure depicts the setup and steps for measuring the ion transport in the thin MoS_2 film. The left panel indicates a EIS measurement prior to intercalation of Li^+, the middle panel indicates the intercalation process with a droplet of $LiClO_4$ solution as the lithium-ion source, and the right panel is the Li^+ intercalated MoS_2 being measured by EIS.

The Li^+ is intercalated into the MoS_2 film by applying a 3 V potential across 1.0 M $LiClO_4$ droplet on the surface of the MoS_2 film connected to the two Au electrodes. When the potential is applied, the ClO_4^- anions are shuttled towards the electrode, and the Li^+ is intercalated into the MoS_2 sheets and will act as the lithium-ion source for the ionic conductivity measurements (Figure 3.9). First, we performed EIS on the MoS_2 thin film device with a 50-mV amplitude sinusoidal potential. A linear curve extending in the imaginary impedance as scanning frequency decreases without changes in the real impedance value, and the semicircle appears in the MoS_2 thin film device that has been intercalated with Li^+ (Figure 3.10 a).

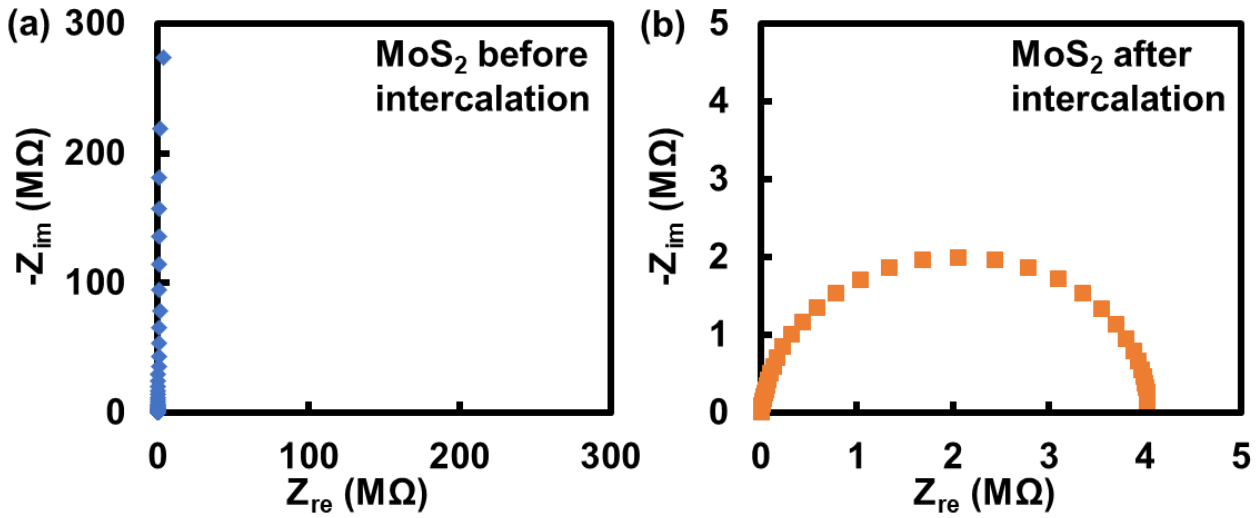

Figure 3.58. The figure consists of (a) EIS measurement of MoS_2 thin film device from 1MHz to 1Hz with 50 mV potential, and then (b) EIS measurement of the same MoS_2 thin film device after intercalation of Li^+ from 1MHz to 1Hz with 50 mV potential. Note the dimension of the thin film were not normalized on the axis.

The MoS_2 thin film device before intercalation has a Nyquist plot that can be well fitted with a resistor in series to a capacitor. The resistor is the resistance of the electron through the circuit. While the long tail extending in the imaginary impedance can be explained as the capacitor in the series. This suggests the device is capacitive in its behavior when subjected to a small voltage of 50 mV. In other words, there are no charge transfer process within the MoS_2 thin film, and thus making it behave like the dielectric material in a capacitor, where the charges are stored at either end of the Au electrodes. Interestingly, after intercalation of Li^+ into the MoS_2 thin film device, we see a change in the Nyquist plot for the device. The Li^+ intercalated MoS_2 thin film device begins to show signs of ion conduction, namely the formation of the semicircle on the Nyquist plot. With a semicircle, that suggests there is a resistive behavior occurring within the 1MHz to 1Hz range, a typical range where ion conduction happens. And we can perform

equivalent circuit fitting using simplified Randles circuit. The simplified Randles circuit is the normal Randles circuit missing the Warburg impedance. From the equivalent circuit fitting, the resistance value of the semicircle suggests the resistance of the ion conduction process as 4.0 MΩ (Figure 3.10 b). And taking in the consideration of the film have a 1.0 cm x 5.0 μm cross section area, and a ion conduction pathway thickness of 1.0 cm. This suggests the ionic conductivity of Li^+ in MoS_2 to be 5 x 10^{-4} S/cm. Which suggests that surface interaction with Li^+ as a promising consideration when designing a solid polymer electrolyte, to utilize both the surface groups and surface area in the case of high surface area material like silica aerogel, hBN aerogel, and MoS_2 nanosheets.

3.4 Conclusion

To summarize, our studies demonstrate that ionic conductivity of solid polymer electrolytes can be improved by utilizing high surface area material with electronegative surface groups. The silica aerogel 3D structure offers both hydroxyl surface groups to stabilize lithium ion during ion conduction as well as high surface area of 810 m^2/g, which means greater surface area of interaction for the lithium ions and achieving ionic conductivity of 2 x 10^{-5} S/cm. Similarly, for hBN aerogel constructed mostly of hBN sheets, the repeating units of boron and nitrogen offers a unique surface potential map for transfer of Li^+ across the surface. In addition, the exceptionally high surface area of 1080 m^2/g enhances further lithium-ion conduction. The hBN aerogel polymer composite electrolyte ultimately achieving ionic conductivity of 5 x 10^{-5} S/cm. Taking the advantage of suitable surface functional group and high surface area idea, we went a step further with the MoS_2 nanosheet thin film, which provides a 3D structure with mostly unidirectional interface filled with some PVP sandwiched between sulfur atoms, this

provided a more ideal pathway condition of directionality, potential well, and large surface area of interaction. Surprisingly, the ionic conductivity of 5 x 10^{-4} S/cm.

With exceptionally high surface area, ideal surface groups, and directionality control, the ionic conductivity of the solid-state electrolytes can be improved with modification to make them into composite materials. The MoS_2 nanosheet structure or the hBN aerogel 3D nanostructure opens new avenue for enhancing the ionic conductivity of solid-state electrolytes. This would lead to a robust system with both mechanical durability and efficient ion transport and allow the realization of all solid-state lithium metal battery to achieve high energy density and fast recharge.

3.5 Reference

1. Kotobuki, M., Kanamura, K., Sato, Y. & Yoshida, T. Fabrication of all-solid-state lithium battery with lithium metal anode using Al2O3-added Li7La3Zr 2O12 solid electrolyte. *J. Power Sources* **196**, 7750–7754 (2011).

2. Sun, C., Liu, J., Gong, Y., Wilkinson, D. P. & Zhang, J. Recent advances in all-solid-state rechargeable lithium batteries. *Nano Energy* **33**, 363–386 (2017).

3. Gao, Z. *et al.* Promises, Challenges, and Recent Progress of Inorganic Solid-State Electrolytes for All-Solid-State Lithium Batteries. *Adv. Mater.* **30**, 1–27 (2018).

4. Randau, S. *et al.* Benchmarking the performance of all-solid-state lithium batteries. *Nat. Energy* **5**, 259–270 (2020).

5. Sakuda, A., Hayashi, A. & Tatsumisago, M. Sulfide solid electrolyte with favorable

mechanical property for all-solid-state lithium battery. *Sci. Rep.* **3**, 2–6 (2013).

6. Cao, D. *et al.* Lithium Dendrite in All-Solid-State Batteries: Growth Mechanisms, Suppression Strategies, and Characterizations. *Matter* **3**, 57–94 (2020).

7. Hou, G. *et al.* Lithium Dendrite Suppression and Enhanced Interfacial Compatibility Enabled by an Ex Situ SEI on Li Anode for LAGP-Based All-Solid-State Batteries. *ACS Appl. Mater. Interfaces* **10**, 18610–18618 (2018).

8. Ji, X. *et al.* Solid-State Electrolyte Design for Lithium Dendrite Suppression. *Adv. Mater.* **32**, 1–9 (2020).

9. Wang, C. *et al.* Suppression of Lithium Dendrite Formation by Using LAGP-PEO (LiTFSI) Composite Solid Electrolyte and Lithium Metal Anode Modified by PEO (LiTFSI) in All-Solid-State Lithium Batteries. *ACS Appl. Mater. Interfaces* **9**, 13694–13702 (2017).

10. Shen, L. *et al.* Progress on Lithium Dendrite Suppression Strategies from the Interior to Exterior by Hierarchical Structure Designs. *Small* **16**, 1–40 (2020).

11. Wan, J. *et al.* Ultrathin, flexible, solid polymer composite electrolyte enabled with aligned nanoporous host for lithium batteries. *Nat. Nanotechnol.* **14**, 705–711 (2019).

12. Wan, J. *et al.* Status, promises, and challenges of nanocomposite solid-state electrolytes for safe and high performance lithium batteries. *Mater. Today Nano* **4**, 1–16 (2018).

13. Lin, D. *et al.* A Silica-Aerogel-Reinforced Composite Polymer Electrolyte with High Ionic Conductivity and High Modulus. *Adv. Mater.* **30**, 1–8 (2018).

14. Li, Y., Fedkiw, P. S. & Khan, S. A. Lithium/V6O13 cells using silica nanoparticle-based

composite electrolyte. *Electrochim. Acta* **47**, 3853–3861 (2002).

15. Ito, S., Unemoto, A., Ogawa, H., Tomai, T. & Honma, I. Application of quasi-solid-state silica nanoparticles-ionic liquid composite electrolytes to all-solid-state lithium secondary battery. *J. Power Sources* **208**, 271–275 (2012).

16. Zhang, N., He, J., Han, W. & Wang, Y. Composite solid electrolyte PEO/SN/LiAlO 2 for a solid-state lithium battery. *J. Mater. Sci.* **54**, 9603–9612 (2019).

17. Dirican, M., Yan, C., Zhu, P. & Zhang, X. Composite solid electrolytes for all-solid-state lithium batteries. *Mater. Sci. Eng. R Reports* **136**, 27–46 (2019).

18. Anilkumar, K. M., Jinisha, B., Manoj, M. & Jayalekshmi, S. Poly(ethylene oxide) (PEO) – Poly(vinyl pyrrolidone) (PVP) blend polymer based solid electrolyte membranes for developing solid state magnesium ion cells. *Eur. Polym. J.* **89**, 249–262 (2017).

19. Shen, Y. J., Reddy, M. J. & Chu, P. P. Porous PVDF with LiClO4 complex as ‘solid’ and ‘wet’ polymer electrolyte. *Solid State Ionics* **175**, 747–750 (2004).

20. Aziz, S. B., Woo, T. J., Kadir, M. F. Z. & Ahmed, H. M. A conceptual review on polymer electrolytes and ion transport models. *J. Sci. Adv. Mater. Devices* **3**, 1–17 (2018).

21. Marcinek, M. *et al.* Electrolytes for Li-ion transport - Review. *Solid State Ionics* **276**, 107–126 (2015).

22. Devaux, D., Bouchet, R., Glé, D. & Denoyel, R. Mechanism of ion transport in PEO/LiTFSI complexes: Effect of temperature, molecular weight and end groups. *Solid State Ionics* **227**, 119–127 (2012).

23. Yu, S. & Siegel, D. J. Grain Boundary Contributions to Li-Ion Transport in the Solid

Electrolyte Li7La3Zr2O12 (LLZO). *Chem. Mater.* **29**, 9639–9647 (2017).

24. Uhlmann, C., Braun, P., Illig, J., Weber, A. & Ivers-Tiffée, E. Interface and grain boundary resistance of a lithium lanthanum titanate (Li3xLa2/3-xTiO3, LLTO) solid electrolyte. *J. Power Sources* **307**, 578–586 (2016).

25. Xu, X. *et al.* Elastic ceramic aerogels for thermal superinsulation under extreme conditions. *Mater. Today* **42**, 162–177 (2021).

26. Xu, X. *et al.* Double-negative-index ceramic aerogels for thermal superinsulation. *Science (80-.).* **363**, 723–727 (2019).

27. Lin, D. *et al.* High Ionic Conductivity of Composite Solid Polymer Electrolyte via in Situ Synthesis of Monodispersed SiO2 Nanospheres in Poly(ethylene oxide). *Nano Lett.* **16**, 459–465 (2016).

28. Mohanta, J., Singh, U. P., Panda, S. K. & Si, S. Enhancement of Li+ ion conductivity in solid polymer electrolytes using surface tailored porous silica nanofillers. *Adv. Nat. Sci. Nanosci. Nanotechnol.* **7**, (2016).

29. Rudolph, W., Brooker, M. H. & Pye, C. C. Hydration of lithium ion in aqueous solution. *J. Phys. Chem.* **99**, 3793–3797 (1995).

30. Pye, C. C., Tomney, M. R. & Enright, T. G. An Ab initio investigation of lithium ion hydration III. Revisiting hydration and the halide ion pair. *Can. J. Anal. Sci. Spectrosc.* **50**, 344–353 (2005).

31. Śmiechowski, M., Gojlo, E. & Stangret, J. Ionic hydration in LiPF6, NaPF6, and KPF6 aqueous solutions derived from infrared HDO spectra. *J. Phys. Chem. B* **108**, 15938–

15943 (2004).

Chapter 4. Solid Composite Electrolyte with Percolating Ionic Conductive Network for Ultrahigh Energy Density Lithium Batteries

4.1 Introduction

Lithium metal anodes are promising higher energy density batteries for portable electronic devices and electrical vehicles.[1,2] However, the implementation of Li metal in commercially batteries is hindered by their undesirable dendrite growth due to repeated charging/discharging cycles.[3,4] Such lithium dendrites often penetrate the microporous polyethylene/polypropylene separators, leading to internal shorts and catastrophic failure.[5–9] The fundamental problem with dendrite penetration is due to the insufficient Young's modulus (10 - 100 MPa) of these polymer separators,[10–14] which inadequately compete against the modulus of lithium dendrites, which is in the order of 10 GPa.[15,16] Despite the frailty of separators, their geometry needs to be kept thin in order to promote ion transport and minimize the resistance of higher discharge currents.[15,16] The overall issue presents itself as a logical quandary, where improvements in performance through the reduction of thickness compromise the safety and reliability of the battery.

Solid-state electrolytes (SSEs) offer a potential solution to this challenge due to their intrinsically high Young's modulus (100 – 10,000 MPa) when compared to liquid electrolyte separators.[17–21] The use of higher modulus solid state electrolytes may also allow for thinner separation distances between the cathode and anode, thus enhancing Li ion transport rates. In addition, a solid state electrolyte also serves as a potential replacement for its more flammable liquid counterpart.[22,23]

A wide variety of solid-state electrolytes have been explored for energy storage devices, which can be largely categorized as either inorganic or organic solid electrolytes.[24–26] Inorganic solid electrolytes such as lithium lanthanum zirconium oxide garnet (LLZO), or lithium lanthanum titanium oxide perovskite (LLTO), exhibit high lithium ionic conductivity but suffer from poor electrode-electrolyte contact; they often require binders, which lower bulk ionic conductivity.[27–30] On the other hand, organic solid electrolytes such as polymer electrolytes show promising flexibility and surface contact, but they are limited in performance through their low ionic conductivity that lies in the range of 10^{-5} to 10^{-8} S/cm.[33–38]

Recently, polymer composite solid-state electrolytes embedded with nanofillers[34–40] have been shown to exhibit improved ionic conductivities in the range of 10^{-4} to 10^{-5} S/cm. Such improvement was attributed to morphological and electrochemical enhancements by the inert nanoparticles. However, the primary lithium-ion conduction pathway is still through the polymer matrix, which limits the kinetics of lithium-ion conduction to the capabilities of the polymer. Although the effects of crystalline polymer disruption by nanofillers are well-studied,[37,38,40] the potential of a fully percolating pathway for Li ion transport has yet to be fully considered.

Rather than complicate the current syntheses for these nanocomposite materials, we draw inspiration from the interface of interactions between water and solid surfaces. The interfacial interactions between the two materials are due to interfacial tension and wettability. This understanding of favorable wettability inspired us to utilize the interface between two solids to create a percolating pathway for efficient transport of materials in nanocomposites. Thus, percolation theory inspired us to study ionic conductivity of lithium ions in solid nanocomposites that originate from the interfacial ion transport mechanism. To achieve this, the nanocomposite in this work has tailored interfacial chemistry for lithium-ion conduction.

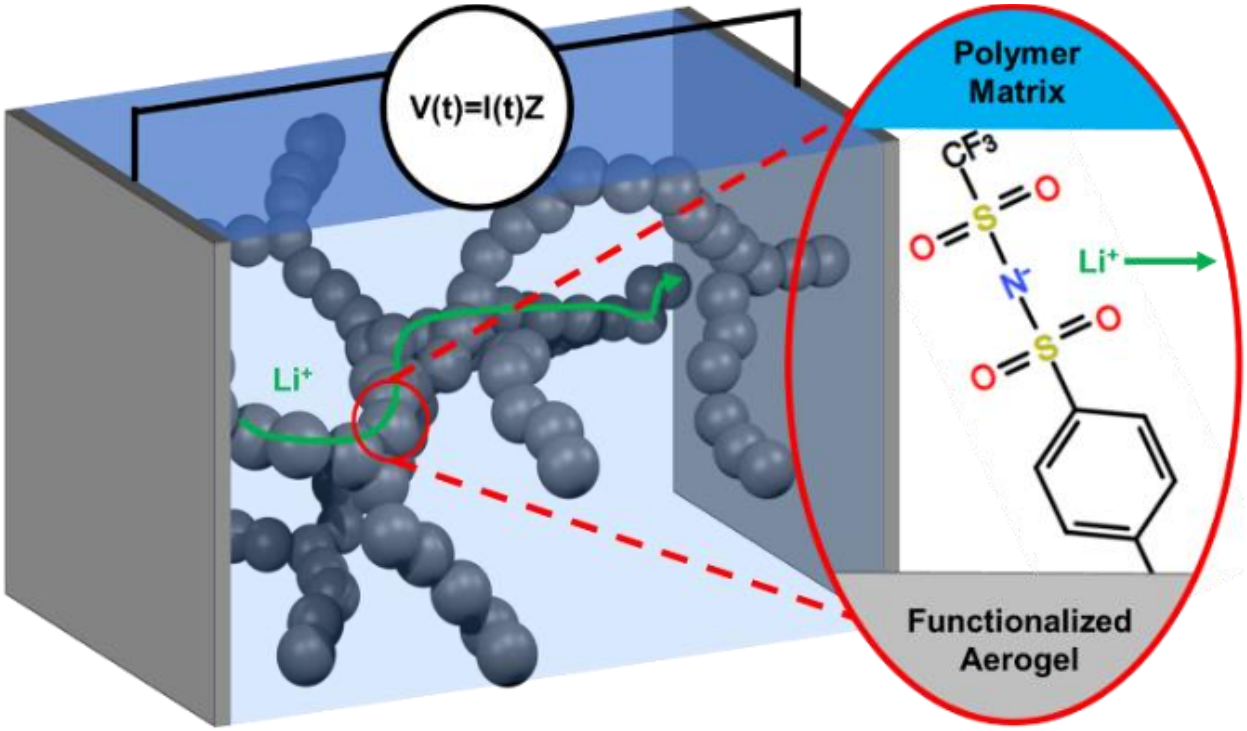

Figure 4.59. The figure demonstrates the concept of improving lithium-ion conduction in the composite solid polymer electrolyte sandwiched between two stainless steel plates (SS) with EIS being tested. The inset shows the surface functional group to interact with Li^+ on the interface between polymer matrix and silica aerogel surface.

Lithium (Li) metal batteries are promising for ultrahigh energy density storage. A persistent challenge that prevents the industrial adoption of Li metal batteries is the formation of lithium-dendrites that could pierce through the separator to cause short-circuit and catastrophic failure. Solid electrolytes can mitigate the risk of lithium-dendrite penetration and presents a potential solution. However, solid electrolytes are generally limited by insufficient ionic conductivity. Herein we investigate the effect of interface chemistry in tailoring the ionic transport in a silica aerogel/polymer composite electrolyte. In this design, lithium trifluoromethane-bis-

(sulfonyl)imide (LiTFSI) surface functionalized silica aerogel/polyethylene oxide (PEO) composite was made to enhance Li^+ transport. The functionalized composite electrolyte shows greatly improved ionic conductivity up to $2x10^{-3}$ S/cm. We further show the composite exhibits attractive ion transport properties in the ultralow temperature regime below -60 ^oC. This study opens a new avenue to tailoring interface chemistry in solid state composite electrolytes for high ionic conductivity.

Herein, we demonstrate a solid-state nanocomposite electrolyte featuring a percolating interfacial network with tailored interface chemistry for efficient Li ion transport (Figure 4.1). we demonstrate that anionic functional groups on the silica aerogel surface allow for systematic tailoring of ionic conductivity. We show that favorable surface chemistry of LiTFSI functionalized silica aerogel dramatically increases Li ion conductivity from 10^{-4} S/cm to 10^{-3} S/cm. This large increase in ionic conductivity is attributed to a highly interconnected percolating network with proper interfacial chemistry. Lastly, we demonstrate the low temperature stability of solid-state composite electrolytes in temperature regimes where conventional liquid electrolytes cannot function.

4.2 Experimental

The functionalization agent triethylammonium 2-[(trifluoromethanesulfonylimido)-N-4-sulfonylphenyl]-ethyl-trimethoxysilane (TFSIS) was synthesized by solvothermal reaction in dichloromethane. A typical synthesis starts with dissolving 0.71 mg of trifluoromethanesulfonamide (TFSN) in a mixture of 20 mL dichloromethane and 3.3 mL of triethylamine for 15 minutes. The resulting mixture was then sealed, freeze pump thawed and

backfilled with argon. Then, 1.1 mL of a 50% solution of 2-(4-chlorosulfonylphenyl)ethyltrimethoxysilane, in dichloromethane was diluted with 10 mL of dichloromethane in the argon glovebox. The silane mixture was then introduced into the TFSN mixture via cannula under air free conditions. The combined mixture was then heated and stirred at 40 °C under argon overnight. The resulting TFSIS solution is dark brown and clear.

The synthesis of silica aerogel starts with a prepared base solution of 1.85 g of NH_4F in a solution of 22.8 mL of NH_4OH 28% solution in water and 100 mL of water, and a precursor solution of 5.0 mL tetraethoxysilane (TEOS) in 11 mL ethanol. Then 370 mL of base solution was mixed with 7.0 mL water and 11 mL ethanol followed by 16 mL of precursor solution. The mixture was then stirred for 2 minutes before 2.5 mL of the mixture is poured into a 2 cm cylindrical polyisoprene mold to set for 30 minutes before a free standing solgel is formed. The solgel is then placed into an ethanol bath to be solvent exchanged before being placed in a supercritical dryer to yield the silica aerogel.

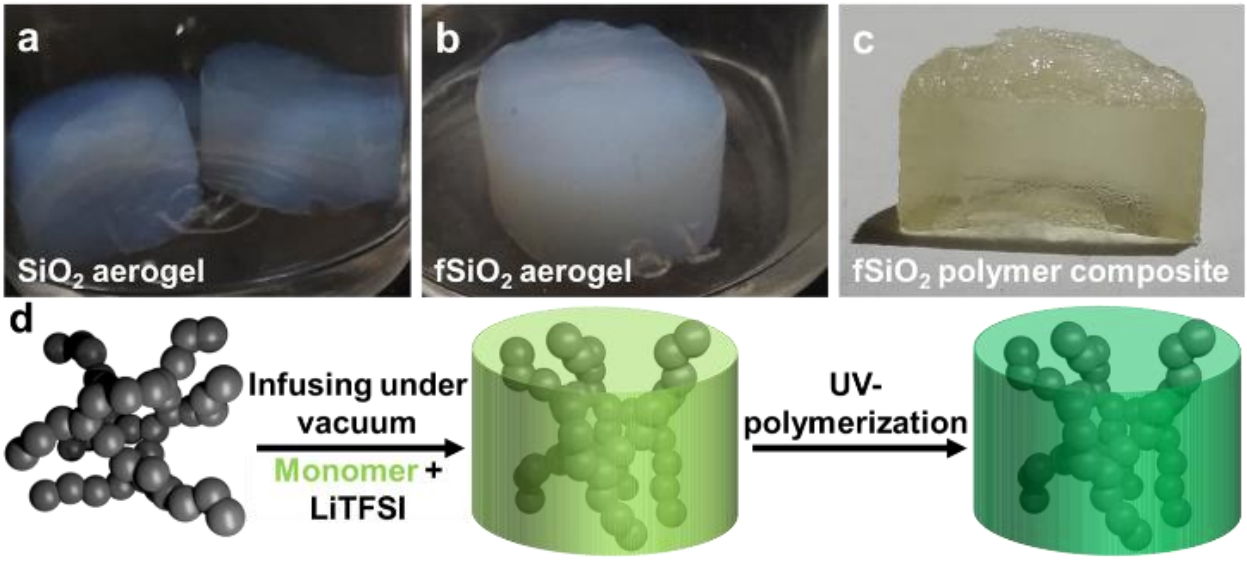

Figure 4.60. (a) Image of silica aerogel. (b) Image of functionalized silica aerogel. (c) Image of functionalized silica aerogel-polymer composite with cross section shown in front. (d)

Schematic representation of the synthesis of functionalized silica aerogel network based solid polymer electrolyte composite.

The as-is synthesized silica aerogel and surface functionalized silica aerogel are shown in Figure 4.2 a,b. To form the functionalized aerogel, When the solgel was formed, 50 μL of TFSIS solution was diluted with 100 mL ethanol and 10 mL of the diluted solution was used to fully submerge the free-standing aerogel in a glass vial. The solgel was left in the functionalizing solution for 3 hours, followed by submersion in a 1 M $LiClO_4$ in ethanol solution for 1 day to exchange Li ions onto the functional group. Subsequent washing of the solgel by soaking in fresh 50 mL acetone every 12 hours for 4 days before being placed in a supercritical dryer produced the functionalized silica aerogel.

The synthesis of the functionalized ($fSiO_2$) and non-functionalized silica (SiO_2) polymer composite starts with 5.6 g of polyethylene glycol diacrylate (PEGDA) with average Mn ~700 mixed with 3.7 g of butanedinitrile, 4.2 g of Bis(trifluoromethylsulfonyl)amine lithium salt (LiTFSI) and 56 mg of phenylbis(2,4,6-trimethyl-benzoyl) phosphine oxide photoinitiator to form the monomer solution. The respective silica aerogel was then submerged in the monomer solution and placed in a vacuum chamber to infuse the aerogel with the monomer solution for 1 hour. The resulting material was a free-standing monomer electrolyte and aerogel composite (Figure 4.2. d). The composite is then placed under a 254 nm ultraviolet lamp for 20 minutes to crosslink PEGDA to form polyethylene oxide (PEO), resulting in a free-standing aerogel/polymer composite electrolyte (Figure 4.2. c,d). All steps for monomer solution preparation prior to photocuring are enclosed in a dark vial to prevent external light sources from photopolymerizing the monomer prior to photocuring process.

Solid-state cross-polarization magic angle spinning carbon–13 nuclear magnetic resonance (CP/MAS ^{13}C NMR) spectra were obtained on a Bruker AV600 using a 3.2 mm zirconia rotor spinning at 18 kHz with 1024 scans. Solid-state Raman spectroscopy was performed on the functionalized silica aerogel with LabRAM HR Evolution Raman spectrometer by Horiba Scientific with an excitation laser at 488 nm and a detection range of 100 cm^{-1} to 3000 cm^{-1}.

Electrochemical measurements were performed on cross section slices of the silica aerogel/polymer composite electrolyte using an electrochemical workstation CHI-790E. The solid electrolyte is pressed between two glass slides with sputtered Ti/Au (50 nm/50 nm) thin film to form a symmetrical cell. Then electrochemical impedance spectroscopy (EIS) is performed at 50 mV in the frequency range of 1MHz to 1Hz. The resulting impedance data is transformed into a Nyquist plot for equivalent circuit fitting by Randle's circuit, to evaluate the bulk resistance (R_{bulk}) of the composite electrolyte and fitted R_{bulk} is used to calculate ionic conductivity according to Eq (5). The surface area is measured with a digital camera and evaluated with the ImageJ program, while the thickness is measured by a digital caliper with a resolution down to 10 µm.

4.3 Results and Discussions

To confirm the presence of TFSI groups on the silica aerogel surface, solid state ^{13}C NMR was utilized. The functionalized aerogel was taken and crushed into a powder to ensure uniform sampling. ^{13}C NMR peaks at 29 and 122–130 ppm indicate the presence of aliphatic and aromatic carbons, respectively (Figure 4.3. a). This allowed us to confirm the surface was functionalized and no precursor solution remained.

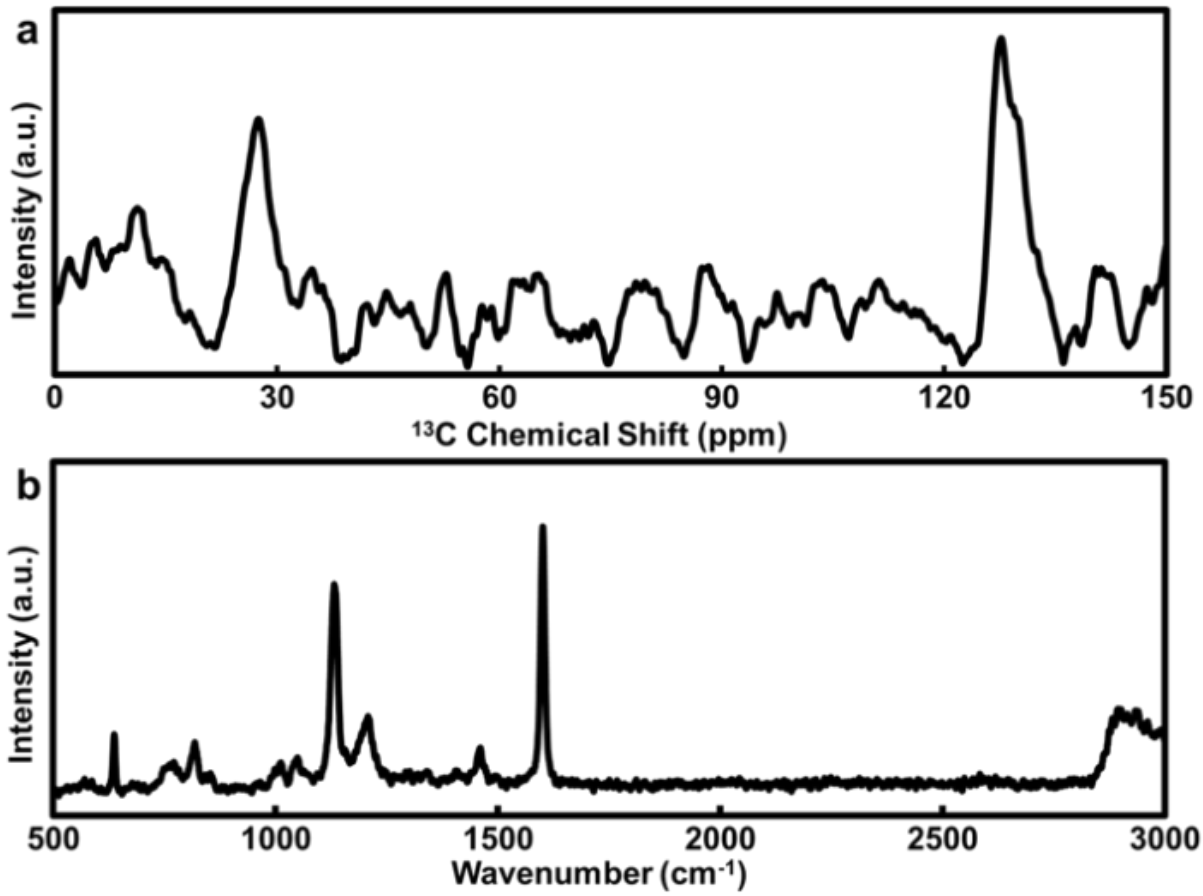

Figure 4.61. (a) Solid state CP/MAS ^{13}C NMR spectrum of functionalized silica aerogel ($fSiO_2$). (b) Solid state Raman spectroscopy of functionalized silica aerogel ($fSiO_2$).

Furthermore, solid-state Raman spectroscopy was conducted on the functionalized aerogel powder (Figure 4.3. b). The C–F stretch of the TFSI trifluoromethyl group corresponds to the peak at 762 cm^{-1}. Further peaks at 820 cm^{-1} and the broad peak around 2900–3000 cm^{-1} are identified as the sp^3 C–H and aromatic ring sp^2 C–H stretches, with the signal at 820 cm^{-1} resulting from the out-of-plane bending mode for the 1,4-disubstituted benzene ring. The peaks at 1052 cm^{-1} and 1461 cm^{-1} are identified as residual triethylamine leftover from synthesis. The 1134 cm^{-1} and 1208 cm^{-1} absorptions are identified as the two different sulfonamide S–O bonds present in TFSI.

With confirmation that the aerogel was indeed functionalized, we moved to examine the ionic conductivity of the functionalized aerogel network in the solid polymer composite electrolyte. A 1.00 mm thin slice of the composite solid electrolyte was cut and sandwiched between two Au sputtered slides to form Au/SSE/Au symmetrical cells. AC impedance spectroscopy was conducted with a frequency range of 1MHz to 1Hz and fit using Nyquist plots (Figure 4.4 a,b). Without surface functionalization, the silica aerogel (SiO_2) composite shows an ionic conductivity of 3.0 x 10^{-4} S/cm, which is comparable to previous studies on a similar composite.[20] Significantly, the functionalized silica aerogel ($fSiO_2$) composite shows an ionic conductivity of 2.0 x 10^{-3} S/cm, with an order magnitude improvement in ion conduction.

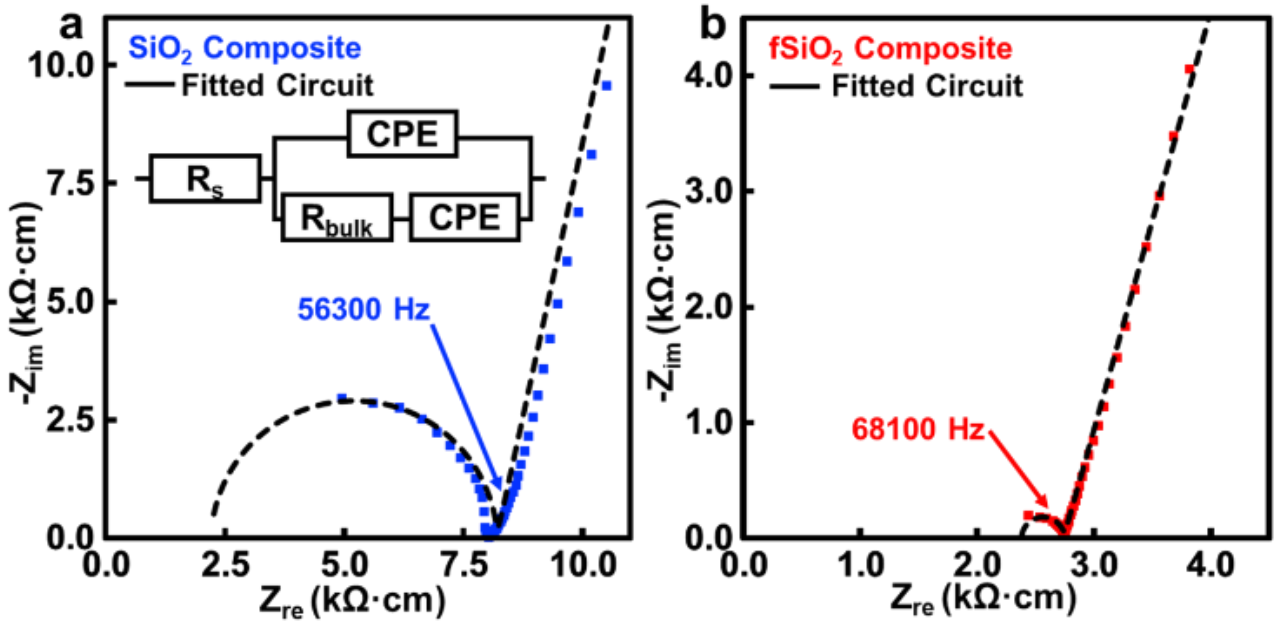

Figure 4.62. Nyquist plot of (a) SiO_2 - PEO composite (blue) with inset equivalent circuit used for measuring R_{bulk} and (b) f-SiO_2 – PEO composite (red), measured with the same equivalent circuit.

To our knowledge, few polymer electrolytes have ionic conductivities exceeding 10^{-3} S/cm at room temperature. Typical polymer electrolytes such as PEO solid state electrolyte have ionic conductivities of 10^{-5} S/cm, and polyvinylidene fluoride (PVDF) solid electrolyte has an ionic conductivity up to 7.0 x 10^{-4} S/cm (Figure 4.5). Incorporation of nano-fillers such as 0D SiO_2 nanoparticles and 1D ZrO_2 nanowires have been used previously with moderate ionic conductivity improvement up to 4 x 10^{-5} S/cm. By using aligned lithium lanthanum titanium oxide perovskite (LLTO) nanowires or SiO_2 aerogel nanostructures, the ionic conductivity improves by an order of magnitude to 6.0 x 10^{-4} S/cm (Figure 4.5). However, such improvement falls short of the prevalent commercial electrolyte ionic conductivities of 10^{-3} to 10^{-4} S/cm. In contrast, our fSiO_2 composite performs on par with commercial electrolytes, displaying an ionic conductivity of 2.0 x 10^{-3} S/cm, a 2-orders of magnitude increase over pure PEO electrolyte.

Figure 4.5. Comparison of ionic conductivity in mS/cm between PEO solid electrolyte and polymer electrolyte with additives of doped ZrO_2 nanowires, SiO_2 nanoparticles, aligned LLTO nanowires, SiO_2 aerogel and fSiO_2 polymer composite.[20,41–44]

We have further measured ionic conductivity in SS/SSE/SS coin cell across wide range of temperature from 65ºC to -100ºC to derive the activation energy and explore the ionic conduction mechanism. The measured ionic conductivity is then plotted as Arrhenius plot, where the activation energy can be extracted and compared (Figure 4.6). The functionalized silica aerogel composite exhibits a low activation energy of 0.24 eV.

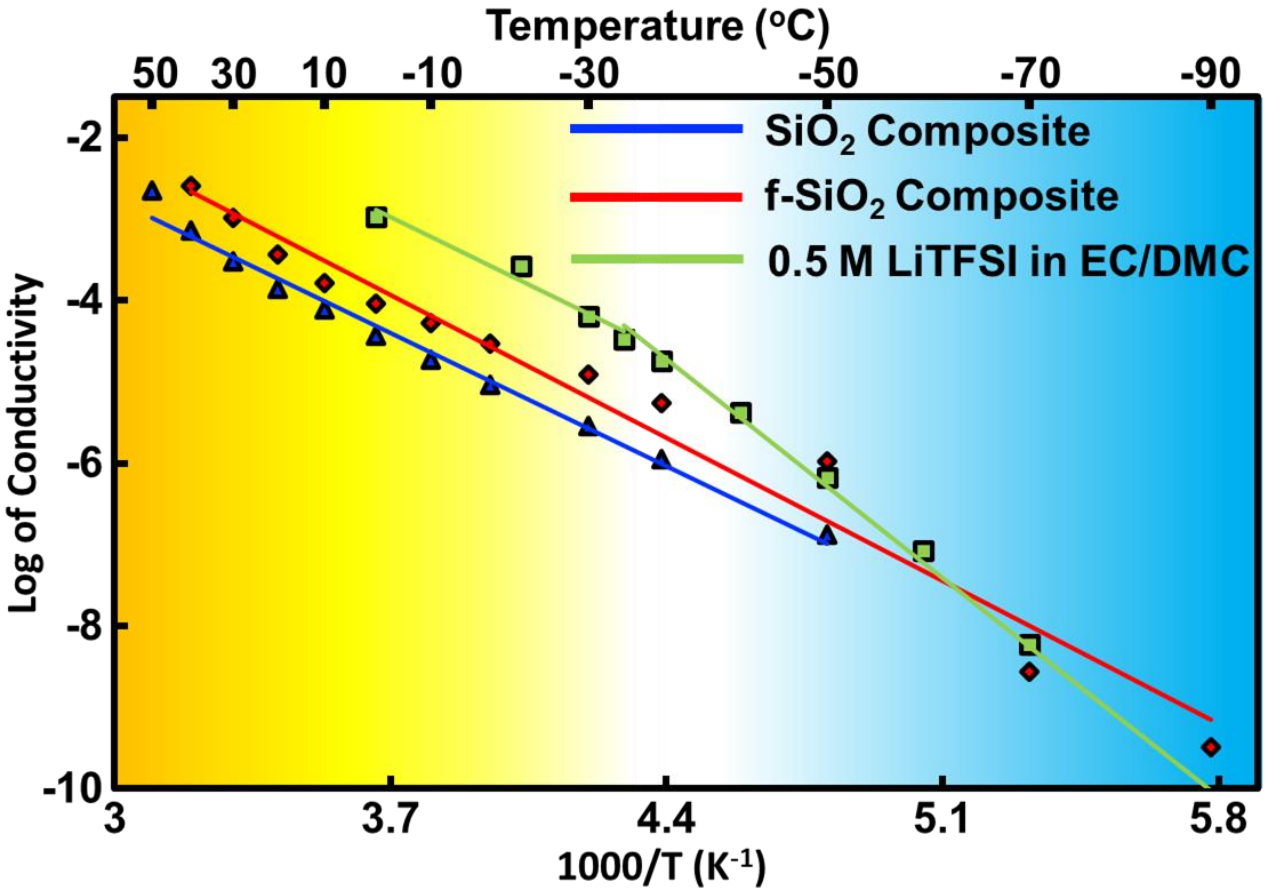

Figure 4.6. The graph shows the temperature dependence of ionic conductivity in various electrolytes. Silica electrolyte composite, functionalized silica composite and standard EC/DMC electrolyte are compared in a testing temperature range from 50 ºC to -65 ºC.

To our surprise, when comparing the Arrhenius plot of composite solid electrolyte to the commercial 1 M LiTFSI EC/DMC 1:1 electrolyte, a more consistent trend is observed in the

composite electrolyte. This is due to the lack of phase change in our composite electrolyte, while the commercial liquid electrolyte shows a rapid decline in ionic conductivity below -35 ºC. This is likely due to the freezing of the solvent, which is a physical disadvantage of the liquid electrolyte. The decline of ionic conductivity of liquid electrolyte below the -35 ºC point is much faster compared to that solid electrolyte.

To take a step further in our temperature measurement, we extended the low temperature range of ionic conductivity measurements down to -100 ºC. It was observed that at -77 ºC, the ionic conductivity of solid-state electrolyte outperforms the organic liquid electrolyte, which is frozen into a solid with lower ionic conductivity (Figure 4.6). Though the ionic conductivity remains low, it is paramount to point out the lack of phase change from the wide temperature range of the solid composite electrolyte leads to a nearly constant change of ionic conductivity depending on the temperature, in stark contrast to liquid electrolytes with much more rapid decrease of ionic conductivity with reducing temperature.

4.4 Conclusion

We have reported a new class of nanocomposite solid-state electrolyte with a complete interfacial percolation network and tailored interfacial chemistry for optimized Li ion transport. This solid-state nanocomposite electrolyte has been synthesized with silica aerogel surface functionalization with LiTFSI and polyethylene oxide chemistries. We show a high ionic conductivity of $2x10^{-3}$ S/cm was achieved in the composite solid electrolyte, which rivals that of gel and liquid electrolytes. To take a further step, we examine the typically ignored low temperature region when considering ionic conductivity, and to our surprise, due to the stable structure and

lack of phase change property of the solid, the ionic conductivity of the solid overtakes that of typical liquid electrolyte at the low temperature extreme. The solid-state nanocomposite electrolyte has the essential properties that makes itself promising for future Li metal battery.

4.5 Reference

1. Xu, R. *et al.* Artificial Soft–Rigid Protective Layer for Dendrite-Free Lithium Metal Anode. *Adv. Funct. Mater.* **28**, 1–7 (2018).

2. Wood, K. N., Noked, M. & Dasgupta, N. P. Lithium metal anodes: Toward an improved understanding of coupled morphological, electrochemical, and mechanical behavior. *ACS Energy Lett.* **2**, 664–672 (2017).

3. Cheng, X. B. & Zhang, Q. Dendrite-free lithium metal anodes: Stable solid electrolyte interphases for high-efficiency batteries. *J. Mater. Chem. A* **3**, 7207–7209 (2015).

4. Cheng, X. B. *et al.* Implantable Solid Electrolyte Interphase in Lithium-Metal Batteries. *Chem* **2**, 258–270 (2017).

5. Bai, P. *et al.* Interactions between Lithium Growths and Nanoporous Ceramic Separators. *Joule* **2**, 2434–2449 (2018).

6. Liu, K. *et al.* Extending the Life of Lithium-Based Rechargeable Batteries by Reaction of Lithium Dendrites with a Novel Silica Nanoparticle Sandwiched Separator. *Adv. Mater.* **29**, 1–6 (2017).

7. Liu, Y. *et al.* Making Li-metal electrodes rechargeable by controlling the dendrite growth direction. *Nat. Energy* **2**, 1–10 (2017).

8. Wu, H., Zhuo, D., Kong, D. & Cui, Y. Improving battery safety by early detection of internal shorting with a bifunctional separator. *Nat. Commun.* **5**, 1–6 (2014).

9. Jana, A., Ely, D. R. & García, R. E. Dendrite-separator interactions in lithium-based batteries. *J. Power Sources* **275**, 912–921 (2015).

10. Monroe, C. & Newman, J. The Impact of Elastic Deformation on Deposition Kinetics at Lithium/Polymer Interfaces. *J. Electrochem. Soc.* **152**, A396 (2005).

11. Panday, A. *et al.* Effect of molecular weight and salt concentration on conductivity of block copolymer electrolytes. *Macromolecules* **42**, 4632–4637 (2009).

12. Cheng, X. B., Peng, H. J., Huang, J. Q., Wei, F. & Zhang, Q. Dendrite-free nanostructured anode: Entrapment of lithium in a 3D fibrous matrix for ultra-stable lithium-sulfur batteries. *Small* **10**, 4257–4263 (2014).

13. Maitra, M. G. *et al.* Ion-conductivity and Young's modulus of the polymer electrolyte PEO-ammonium perchlorate. *Solid State Ionics* **178**, 167–171 (2007).

14. Barai, P., Higa, K. & Srinivasan, V. Lithium dendrite growth mechanisms in polymer electrolytes and prevention strategies. *Phys. Chem. Chem. Phys.* **19**, 20493–20505 (2017).

15. Love, C. T. Perspective on the mechanical interaction between lithium dendrites and polymer separators at low temperature. *J. Electrochem. Energy Convers. Storage* **13**, 1–5 (2016).

16. Halalay, I. C., Lukitsch, M. J., Balogh, M. P. & Wong, C. A. Nanoindentation testing of separators for lithium-ion batteries. *J. Power Sources* **238**, 469–477 (2013).

17. Fu, K. *et al.* Three-dimensional bilayer garnet solid electrolyte based high energy density

lithium metal-sulfur batteries. *Energy Environ. Sci.* **10**, 1568–1575 (2017).

18. McGrogan, F. P. *et al.* Compliant Yet Brittle Mechanical Behavior of Li2S–P2S5 Lithium-Ion-Conducting Solid Electrolyte. *Adv. Energy Mater.* **7**, 1–5 (2017).

19. Schulze, M. W., McIntosh, L. D., Hillmyer, M. A. & Lodge, T. P. High-modulus, high-conductivity nanostructured polymer electrolyte membranes via polymerization-induced phase separation. *Nano Lett.* **14**, 122–126 (2014).

20. Lin, D. *et al.* A Silica-Aerogel-Reinforced Composite Polymer Electrolyte with High Ionic Conductivity and High Modulus. *Adv. Mater.* **30**, 1–8 (2018).

21. Sakuda, A., Hayashi, A. & Tatsumisago, M. Sulfide solid electrolyte with favorable mechanical property for all-solid-state lithium battery. *Sci. Rep.* **3**, 2–6 (2013).

22. Nagao, M., Hayashi, A. & Tatsumisago, M. Fabrication of favorable interface between sulfide solid electrolyte and Li metal electrode for bulk-type solid-state Li/S battery. *Electrochem. commun.* **22**, 177–180 (2012).

23. Mizuno, F., Hayashi, A., Tadanaga, K., Minami, T. & Tatsumisago, M. All-solid-state lithium secondary batteries using a layer-structured LiNi0.5Mn0.5O2 cathode material. *J. Power Sources* **124**, 170–173 (2003).

24. Manthiram, A., Yu, X. & Wang, S. Lithium battery chemistries enabled by solid-state electrolytes. *Nat. Rev. Mater.* **2**, 1–16 (2017).

25. Zhao, Q., Stalin, S., Zhao, C. Z. & Archer, L. A. Designing solid-state electrolytes for safe, energy-dense batteries. *Nat. Rev. Mater.* **5**, 229–252 (2020).

26. Famprikis, T., Canepa, P., Dawson, J. A., Islam, M. S. & Masquelier, C. Fundamentals of

inorganic solid-state electrolytes for batteries. *Nat. Mater.* **18**, 1278–1291 (2019).

27. Bachman, J. C. *et al.* Inorganic Solid-State Electrolytes for Lithium Batteries: Mechanisms and Properties Governing Ion Conduction. *Chem. Rev.* **116**, 140–162 (2016).

28. Banerjee, A., Wang, X., Fang, C., Wu, E. A. & Meng, Y. S. Interfaces and Interphases in All-Solid-State Batteries with Inorganic Solid Electrolytes. *Chem. Rev.* acs.chemrev.0c00101 (2020). doi:10.1021/acs.chemrev.0c00101

29. Li, J. *et al.* A promising composite solid electrolyte incorporating LLZO into PEO/PVDF matrix for all-solid-state lithium-ion batteries. *Ionics (Kiel).* **26**, 1101–1108 (2020).

30. Kwon, W. J. *et al.* Enhanced Li+ conduction in perovskite Li3XLa2/3-x□1/3-2xTiO3 solid-electrolytes via microstructural engineering. *J. Mater. Chem. A* **5**, 6257–6262 (2017).

31. Rajendran, S., Sivakumar, M. & Subadevi, R. Li-ion conduction of plasticized PVA solid polymer electrolytes complexed with various lithium salts. *Solid State Ionics* **167**, 335–339 (2004).

32. Sun, B., Mindemark, J., Edström, K. & Brandell, D. Polycarbonate-based solid polymer electrolytes for Li-ion batteries. *Solid State Ionics* **262**, 738–742 (2014).

33. Michael, M. S., Jacob, M. M. E., Prabaharan, S. R. S. & Radhakrishna, S. Enhanced lithium ion transport in PEO-based solid polymer electrolytes employing a novel class of plasticizers. *Solid State Ionics* **98**, 167–174 (1997).

34. Schroers, M., Kokil, A. & Weder, C. Solid polymer electrolytes based on nanocomposites of ethylene oxide-epichlorohydrin copolymers and cellulose whiskers. *J. Appl. Polym. Sci.*

93, 2883–2888 (2004).

35. Boaretto, N., Meabe, L., Martinez-Ibañez, M., Armand, M. & Zhang, H. Review—Polymer Electrolytes for Rechargeable Batteries: From Nanocomposite to Nanohybrid. *J. Electrochem. Soc.* **167**, 070524 (2020).

36. Wan, J. *et al.* Ultrathin, flexible, solid polymer composite electrolyte enabled with aligned nanoporous host for lithium batteries. *Nat. Nanotechnol.* **14**, 705–711 (2019).

37. Zhu, Q., Wang, X. & Miller, J. D. Advanced Nanoclay-Based Nanocomposite Solid Polymer Electrolyte for Lithium Iron Phosphate Batteries. *ACS Appl. Mater. Interfaces* **11**, 8954–8960 (2019).

38. Kwon, S. J. *et al.* Influence of Al2O3 Nanowires on Ion Transport in Nanocomposite Solid Polymer Electrolytes. *Macromolecules* **51**, 10194–10201 (2018).

39. Croce, F., Appetecchi, G. B., Persi, L. & Scrosati, B. (Al2O3, TiO2) Nanocomposite polymer electrolytes for lithium batteries, F. Croce, B. Scrosati, Nature (1998). *Nat. Lett.* **394**, 456–458 (1998).

40. Polu, A. R. & Rhee, H. W. Nanocomposite solid polymer electrolytes based on poly(ethylene oxide)/POSS-PEG (n=13.3) hybrid nanoparticles for lithium ion batteries. *J. Ind. Eng. Chem.* **31**, 323–329 (2015).

41. Lin, D. *et al.* High Ionic Conductivity of Composite Solid Polymer Electrolyte via in Situ Synthesis of Monodispersed SiO2 Nanospheres in Poly(ethylene oxide). *Nano Lett.* **16**, 459–465 (2016).

42. Liu, W., Lin, D., Sun, J., Zhou, G. & Cui, Y. Improved Lithium Ionic Conductivity in

Composite Polymer Electrolytes with Oxide-Ion Conducting Nanowires. *ACS Nano* **10**, 11407–11413 (2016).

43. Liu, W. *et al.* Enhancing ionic conductivity in composite polymer electrolytes with well-aligned ceramic nanowires. *Nat. Energy* **2**, 1–7 (2017).

44. Liu, W. *et al.* Ionic Conductivity Enhancement of Polymer Electrolytes with Ceramic Nanowire Fillers. *Nano Lett.* **15**, 2740–2745 (2015).

Chapter 5. Conclusion

5.1 Conclusion

Exploring the existing battery technology has led to the convergence of a market's dependence on lithium-ion batteries. While the 150 W h/kg specific energy for the lithium-ion battery remains the dominant capacity for the battery technology, for more complex energy requirement of electric vehicles and mobile phones, transition to Li metal battery with the advances in solid state electrolytes is emerging. In the first chapter, a detailed discussion on the different types for electrolytes, liquid electrolytes, organic solid electrolytes, inorganic solid electrolytes, and composite solid electrolytes, each having their merits and shortfalls. Namely, the lack of ionic conductivity for solid state electrolytes as the limiting factor preventing their dominance in the battery technology. So, we explored the factors that affect ionic conductivity as well as methods and techniques used to measure those factors.

In the second chapter, we attempted to create a 3D network of liquid electrolyte encased in surface functionalized mesoporous silica nanoparticle inside of a polymer electrolyte through percolation theory. Using contact angle measurements, we confirmed the ability of the functionalized nanoparticle to store $LiClO_{4(aq)}$ in the hydrophilic mesopores and trap the liquid electrolyte with the hydrophobic outer shell. Furthermore, we measured the ionic conductivity of the functionalized mesoporous silica nanoparticle in polyethylene oxide matrix to have the ionic conductivity of 1.5×10^{-6} and demonstrated that the simple core-shell encasement of the liquid electrolyte cannot sustain long drying duration.

In the third chapter, we shifted focus from gel polymer electrolyte to all solid-state electrolyte, where we identified the lack of ionic conductivity as the main challenge. To address this, we demonstrated the effects of 3D network of solid-state material with stabilization of

lithium ion during ion conduction by utilizing percolating electronegative atoms on the surface of solid-state ceramic materials. We explored the ability of silica aerogel and hBN aerogel to enhance the ionic conductivity of common PEO/LiTFSI electrolyte by one order of magnitude to 2×10^{-5} and 5×10^{-5}. We further demonstrated the ability of MoS_2 thin film to be able to conduct lithium ion at a high conductivity of 5×10^{-4} S/cm after lithium intercalation.

In the fourth chapter, we demonstrated the ability of surface tailored TFSI functional group on silica aerogel to enhance ionic conductivity of the lithium ion at the interface between silica and PEO matrix with percolation pathway. Where we showed a high ionic conductivity of 2.0×10^{-3} S/cm, which rivals that of gel and liquid electrolytes. In addition to this, we also explored the often-ignored low temperature region for ionic conductivity, where we demonstrated the ionic conductivity of the composite electrolyte overtakes that of liquid electrolytes at low temperature extreme. This leads to the solid-state nanocomposite electrolyte as an essential part for the future of lithium-ion battery technology.